Control of the Mitotic Cleavage Plane by Local Epithelial Topology

Control of the mitotic cleavage plane by local epithelial topology

William T. Gibson[1-2,4-5], James H. Veldhuis[3], Boris Rubinstein[2], Heather N. Cartwright[2], Norbert Perrimon[4], G. Wayne Brodland[3], Radhika Nagpal[5], and Matthew C. Gibson[2,6*]

(1) Program in Biophysics, Harvard University (Cambridge, MA 02138, USA)

(2) Stowers Institute for Medical Research (Kansas City, MO 64110, USA)

(3) Department of Civil and Environmental Engineering, University of Waterloo (Waterloo, ON N2L 3G1, Canada)

(4) Department of Genetics, Howard Hughes Medical Institute, Harvard Medical School (Boston, MA 02115, USA)

(5) School of Engineering & Applied Sciences, Harvard University (Cambridge, MA 02138, USA)

(6) Department of Anatomy and Cell Biology, Kansas University Medical Center (Kansas City 64110, KS)

*Contact: <mg2@stowers.org>

SUMMARY

For nearly 150 years, it has been recognized that cell shape strongly influences the orientation of the mitotic cleavage plane (e.g. Hofmeister, 1863). However, we still understand little about the complex interplay between cell shape and cleavage plane orientation in epithelia, where polygonal cell geometries emerge from multiple factors, including cell packing, cell growth, and cell division itself. Here, using mechanical simulations, we show that the polygonal shapes of individual cells can systematically bias the long axis orientations of their adjacent mitotic neighbors. Strikingly, analysis of both animal epithelia and plant epidermis confirm a robust and nearly identical correlation between local cell topology and cleavage plane orientation *in vivo*. Using simple mathematics, we show that this effect derives from fundamental packing constraints. Our results suggest that local epithelial topology is a key determinant of cleavage plane orientation, and that cleavage plane bias may be a widespread property of polygonal cell sheets in plants and animals.

HIGHLIGHTS

- Neighbor cell topology biases cleavage plane orientation in monolayer cell sheets.
- This “cleavage plane bias” is observed in both plants and animals.
- This effect can be explained by fundamental packing constraints.
- Cleavage plane bias influences global epithelial topology.

INTRODUCTION

The active control of the mitotic cleavage plane is crucial to numerous processes, and the consequences of cleavage plane mis-orientation can be catastrophic, ranging from polycystic kidney disease and organ malformation to tumorogenesis (Baena-Lopez et al., 2005; Fischer et al., 2006; Gong et al., 2004; Quyn et al., 2010; Saburi et al., 2008). Although the control of cleavage plane orientation is usually understood from a molecular viewpoint (Buschmann et al., 2006; Fernandez-Minan et al., 2007; Johnston et al., 2009; Siller and Doe, 2009; Speicher et al., 2008; Thery et al., 2005; Traas et al., 1995; Vanstraelen et al., 2006; Walker et al., 2007; Wright et al., 2009), more than a century of observations show that mitotic cells in both plants and animals tend to divide orthogonal to their geometric long axis as a default mechanism (Gray et al., 2004; Hofmeister, 1863; O'Connell and Wang, 2000; Strauss et al., 2006). In plants, the geometric location of the division plane can be predicted by cytoskeletal structures (Kost and Chua, 2002; Palevitz, 1987; Pickett-Heaps and Northcote, 1966; Sinnott and Bloch, 1940), and biophysical experiments suggest that the cytoskeleton may be involved in the process of orienting the division plane as dictated by cell geometry (Flanders et al., 1990; Goodbody et al., 1991; Katsuta et al., 1990; Lloyd, 1991). Further, in animal cells, recent studies implicate the geometry of cell-matrix adhesions as a key determinant of cleavage plane orientation (Thery et al., 2007; Thery et al., 2005). Cell geometry is thus a

critical determinant of cleavage plane orientation, at both the molecular and biophysical level.

While the regulation of mitotic cleavage plane orientation by geometric cues has been extensively probed in unicellular systems, far less attention has been given to adherent epithelial and epidermal layers. In this context, cell geometry does not exist in isolation, because cell shapes emerge from the combined effects of growth, mitosis, and cellular packing. *A priori*, this complex interplay of biological processes, and the diverse genetic programs that have evolved to control them in plants and animals, would appear to suggest a staggering range of possible cell geometries within an epithelium. However, spatial considerations impose powerful constraints on the shapes of cells in monolayer sheets, from the distribution of polygonal cell types (Rivier et al., 1995) to their neighbor correlations (Peshkin et al., 1991) and relative sizes (Rivier and Lissowski, 1982). Indeed, empirical investigation confirms that many monolayer cell sheets across the plant and animal kingdoms converge on a default equilibrium distribution of cellular shapes, with approximately 45% hexagons, 25% pentagons, and 20% heptagons (Gibson et al., 2006; Korn and Spalding, 1973; Lewis, 1928). Such clear conservation of cellular network architecture raises the question as to whether conserved cellular division mechanisms are responsible for generating such similar packing arrangements of cells, as numerous studies have proposed (Dubertret et al., 1998; Gibson et al., 2006; Korn and Spalding, 1973; Miri and Rivier, 2006; Patel et al., 2009). The strongest evidence to date that common mechanisms are used among plants and animals to generate conserved packing

relationships can be found in the *mitotic shift*, wherein the distribution of mitotic cell shapes is shifted by a single polygon class to have a heptagonal mean, as opposed to a hexagonal mean as seen in interphase cells.

Here, we use computational modeling, experimental observation, and mathematical analysis to report that, as a default property, neighbor cell shape can strongly bias cleavage plane orientation in the monolayer cell sheets of both plants and animals. Intriguingly, we show that this bias increases the structural regularity of an epithelium by increasing the frequency of hexagons. Our analysis indicates that simultaneously, cleavage plane bias is also involved in specifying the mitotic shift. The mechanism through which cleavage plane bias accomplishes these effects is differential side-gaining, whereby dividing cells preferentially cleave their common interfaces with sub-hexagonal cells such as quadrilaterals, and avoid cleaving their common interfaces with super-hexagonal cells such as octagons. Together, our results suggest a common emergent mechanism in plants and animals for the control of tissue-level architecture by packing-mediated control of the mitotic cleavage plane.

RESULTS

The shape of a cell is predicted to be influenced by local topology

In epithelia, the tissue-level architecture at the apical junctions is a contiguous tiling of polygonal cell shapes (Figures 1A and B). This pattern can be described as a simple planar network wherein a cell's number of neighbors (topology) is equivalent to its polygon class (Figure 1B'). To investigate the effect of polygonal cell packing on mitotic cell shape, and by extension, cleavage plane orientation, we tested whether a cell's long axis is systematically influenced by the polygon class of neighboring cells.

To address this, we numerically solved for the minimal energy configuration of a local cellular neighborhood (Prusinkiewicz and Lindenmayer, 1990), defined to be a central mitotic cell (*M*) and its first-order polygonal neighbors. Geometrically, cells were idealized as polygonal prisms with constant height (Figure 1A). For relaxation, cell mechanics were modeled in terms a balance between edge-length tensions, described using ideal springs, and internal pressure, modeled as an ideal gas (Figure 1C). The central mitotic cell, *M*, was a heptagon, consistent with the fact that the average mitotic cell is seven-sided *in vivo* (Aegerter-Wilmsen et al., 2010; Gibson et al., 2006). Parameters were chosen to be uniform for every cell, and initial conditions were arbitrary (Figures 1D-F). Given these choices, the effect of local topology on the shape of the

central cell was an emergent property of the relaxed mechanical network at equilibrium (Figures 1D-F; Figure S1; Extended Experimental Procedures).

To analyze the impact of local topology on the long axis of *M*, we replaced one neighbor hexagon with a single N-sided cell, *N*. Strikingly, inserting any non-hexagonal neighbor induced a clear long axis in *M*, with opposite orientation of the long axis for N<6 versus N>6 (Figures 1D-F; 2A). Specifically, the presence of quadrilateral or pentagonal neighbors induced a long axis parallel to the *NM* interface, while heptagons and octagons induced a long axis orthogonal to interface *NM*. These results suggest that in cell sheets, the orientation of a mitotic cell's longest axis can be strongly influenced by the polygon class of a single neighboring cell. As a consequence of this effect, neighbor cells with fewer sides (such as quadrilaterals and pentagons) tend to lie along the shortest axis of M, which is the location of the presumed cleavage plane.

To test whether this effect was robust under more realistic conditions, we numerically relaxed heterogeneous local neighborhoods that were stochastically generated from the known polygonal cell shape distribution of the *Drosophila melanogaster* wing epithelium (Figure 2B) (Aegerter-Wilmsen et al., 2010; Gibson et al., 2006). Even under these conditions, more than 70% of quadrilateral neighbors were positioned on the central cell's short axis, double the percentage expected by chance (Figure 2C). To quantify this relationship, we defined an acute angle, θ, with respect to the presumed cleavage plane along the central cell's short axis (see Figure 2D). On average, as a function of

increasing θ, the neighbor polygon class in direction θ increased monotonically (Figure 2E). Therefore, even in a heterogeneous context, the topology of a cellular neighborhood robustly and systematically influenced the orientation of the long axis in a central cell.

Cleavage plane bias in the *Drosophila* wing disc

In both plants and animals, cells are thought to divide their long axis by forming a cleavage plane along the short axis of the cell (Hofmeister, 1863; Strauss et al., 2006). If a cell's short axis consistently bisects its cellular neighbors having the fewest sides (Figure 2), then mitotic division planes should be disproportionately biased towards quadrilaterals and pentagons *in vivo*. To test this, we measured the correlation between neighbor cell polygon class and cleavage plane orientation in the *Drosophila* wing imaginal disc (Figure 3A). Here, cell division proceeds through a stereotyped process of cell rounding at the apical epithelial surface (Figures 3B-D;(Gibson et al., 2006)). To define the frequency with which different classes of polygonal neighbors were bisected by the cleavage plane, we examined 420 cells at the cytokinetic stage, which is the most stable and easily scored phase of mitosis (Figure 3E). For each case, we recorded the position of all primary neighboring polygons and computed the frequency with which each polygon class occupied the cleavage plane position (Figures 3F,G).

If the orientation of cell division were random with respect to local topology, approximately 28.6% of any given polygon class would be expected to correlate

with the cleavage plane (two randomly-chosen cells out of seven neighbors). However, in the wing disc, we found that more than 50% of quadrilaterals in the primary neighborhood occupied the division plane position (Figure 3H; *n*=46/83). Further, octagons were anti-correlated with the division plane, and occupied that position with less than 10% probability (*n*=6/77). As predicted by the mechanical model, this cleavage plane bias was monotone decreasing across all polygon types. We conclude that in the *Drosophila* wing disc, the polygonal topology of local neighborhoods strongly influences cleavage plane orientation in mitotic cells.

In order to test the assumption that *Drosophila* wing disc cells actually divide their longest axis, we next performed time-lapse analysis of proliferating *Drosophila* wing discs in *ex vivo* culture (see Movie S1; Experimental Procedures). For each of 198 mitotic cells (Figure 4A), we measured the geometric long axis orientation during both interphase (Figure 4A', far left), and cytokinesis (Figure 4A', far right). We found a strong tendency for cells to follow a long-axis division mechanism, although with moderate noise in the orientation (Figure 4B). This tendency to divide the longest axis correlated with the interphase geometry (Figure 4B), and increased with the cell's interphase elongation ratio (the ratio of the long axis to the short axis; Extended Experimental Procedures). For example, for the 99 cells having an elongation ratio below the median value of 1.68, the average deviation from a long axis-division mechanism was about 33°; by contrast, for the 99 cells having an elongation ratio above the median value, the average deviation was about 21°

(data not shown). This dependence on the relative axis lengths suggests that these cells might be able to adjust their spindle orientations to their newly acquired shapes following mechanical strain, as has been previously reported in cell culture and in vertebrate embryonic cells (Black and Vincent, 1988; Gray et al., 2004; O'Connell and Wang, 2000; Strauss et al., 2006).

To test whether deviation from the long axis division mechanism could explain the discrepancy between our cleavage plane bias predictions and the empirical measurements, we incorporated the measured deviation into our original model (Figure 4C; Extended Experimental Procedures). Interestingly, when the measured deviation was incorporated, the mechanical predictions were significantly improved (compare the red and black curves in Figure 4C), closely matching the empirically measured bias (Figure 4C, blue curve). Therefore, cleavage plane bias is likely to be robust to noise in the cleavage plane mechanism, and may be present even when cell divisions do not perfectly obey a long axis division scheme.

Cleavage plane bias in plant epidermis

Because our original predictions were mechanically motivated (Figures 1 and 2), and are expected to persist even when there is moderate noise in the cleavage plane (Figure 4), we reasoned that cleavage plane bias should be equally likely to appear in plant tissues. To test this, we used data from FT Lewis's classical study of cucumber epidermal cell topology (*Cucumis sativus*) to compute the probability with which an N-sided polygonal cell occupies the

division plane of a mitotic neighbor (Extended Experimental Procedures; Lewis, 1928). Remarkably, in *Cucumis*, the cleavage plane bias was almost indistinguishable from that measured in the *Drosophila* wing disc (Figure 3H). We once again observed strong enrichment for 4-sided cells along the cleavage planes of mitotic cells, while 8-sided cells were underrepresented. In order to verify our inferences from Lewis's data (1928), we also directly examined the relationship between local topology and cellular long axis orientation in the epidermis of *Cucumis* (Figure S3A). From fixed samples of cucumber epidermis, we studied a population of 501 epidermal cells having the same polygonal distribution as the original population of 500 mitotic cells studied by Lewis (1928). Cells were selected in a spatially constrained, impartial manner based solely on polygon class (Extended Experimental Procedures). We next tested whether a naïve long-axis division rule was sufficient to generate cleavage plane bias in *Cucumis*. Based on an ellipse of best fit to each cell's geometry (Figure S3A; Extended Experimental Procedures), we were able to reproduce not only the cleavage plane enrichment observed in Lewis's original data (Figure S3C), but also the inferred cleavage plane bias (Figure S3D). Taken together, our results suggest that cleavage plane bias occurs in polygonal cell sheets as an emergent effect of cell packing, independent of species-specific considerations.

Cleavage plane bias and the topological constraints on cell geometry

The quantitative similarity of cleavage plane bias in plants, animals, and *in silico* suggests the underlying mechanism is geometric, rather than molecular. In fact, fundamental geometric constraints imposed by the internal angles of neighboring polygons are sufficient to explain this phenomenon. For illustration, consider the comparison between a tiling of three hexagons versus two hexagons and a square (Figures 5A and B). From elementary geometry, a square (N=4) has internal angles of 90˚, while the internal angles of a hexagon (N=6) average 120˚ (for an N-sided polygon, average internal angles are 180˚(N-2)/N). In the context of a contiguous layer, the presence of 90˚ internal angles within the square forces the internal angles of the adjacent hexagon to increase to 135˚(Figure 5B). Intuitively, this deformation results in elongation of these hexagons parallel to the interface with the square, thus generating a cellular long axis.

The constraints imposed by the internal angles of one cell upon the long axis of its neighbor can be formalized for the arbitrary case of an N-sided cell, surrounded by N symmetric hexagonal neighbors (Figure 5C). Assume that a mitotic cell, *M*, is situated vertically above cell *N*, resulting in a horizontal interface *NM* of length L. In the simplest case, all side lengths, including L, are equal, and without loss of generality can be set to one. Further, the internal angles α_N and β_M can be computed as a function of N. Using simple trigonometry and exploiting the symmetric configuration of neighbors, we can

solve for the ratio of the horizontal axis, d_m, to the vertical axis, h_m, for the ellipse of best fit to cell *M* (Figure 5C; Extended Experimental Procedures):

$$\frac{d_m}{h_m} \approx \sec\left(\frac{\pi}{N}\right)\sqrt{\sin\left(\frac{\pi}{N}\right)\left(1+\sin\left(\frac{\pi}{N}\right)\right)} \qquad (1)$$

In this framework, the direction of *M*'s short axis (presumed cleavage plane) is described by the ratio d_m:h_m, which the above equation shows is determined by the N value (Figure 5D). Geometrically, the ratio d_m:h_m varies with N because the length d_m decreases for N>6 and increases for N<6 (Figure 5E). Consequently, when N>6 (d_m:h_m<1), d_m forms the short axis parallel to interface *NM*. Conversely, if N<6 (d_m:h_m>1), then h_m forms the short axis, or presumed cleavage plane, in the direction of *N*, perpendicular to the interface *NM*.

Cleavage plane bias is predicted to be robust to side length and cell size differences

Intuitively, differential side lengths of N-sided neighbors would also affect the short axis orientation of *M* (Figure 5F). To analyze the relative contributions of angular constraints versus side lengths, consider the more realistic case when the edge lengths are non-uniform (L≠1). Here, d_m:h_m depends on both N and L (Figure 5D and Extended Experimental Procedures):

$$\frac{d_m}{h_m} \approx \sec\left(\frac{\pi}{N}\right)\sqrt{\sin\left(\frac{\pi}{N}\right)\left(L+\sin\left(\frac{\pi}{N}\right)\right)} \qquad (2)$$

For the simplified case when L=1, the direction of the short axis undergoes a 90° rotation (between horizontal and vertical) when d_m:h_m passes through the value 1, which corresponds to N=6 (*red line*, Figure 5D). Changing the value of L changes the length d_m (Figure 5F), and thus alters the N value at which this transition occurs (*black lines*, Figure 5D). The long axis orientation of *M* is thus determined by the interplay between the polygon class and apposed side length of each neighbor, *N*. In the *Drosophila* wing disc, the value of L fluctuates by about 40% on average (Table 1). Equation (2) predicts that a 40% deviation in L value would change the point of rotation by only a single N value, suggesting that cleavage plane bias should be noisy yet reproducible.

Supporting this analysis, cell size has a surprisingly weak influence compared to polygon class in our mechanical simulations (Figure S4). Consistent with our simulations, based on live imaging analysis of local neighborhoods surrounding dividing cells in the *Drosophila* wing disc epithelium, there was no discernable difference in average area for cells occupying the cleavage plane position (Figure S4D). We conclude that internal angle constraints linked to the polygon class of neighboring cells are likely the dominant cause of cleavage plane bias, with a lesser contribution from the effects of differential side lengths.

Cleavage plane bias is predicted to alter global tissue topology

Numerous recent studies have used mathematical or computational approaches to understand the equilibrium topology of proliferating epithelia (Aegerter-Wilmsen et al., 2010; Cowan and Morris, 1988; Dubertret et al., 1998;

Dubertret and Rivier, 1997; Gibson et al., 2006; Korn and Spalding, 1973; Miri and Rivier, 2006; Patel et al., 2009). Intuitively, cleavage plane bias must alter the topology of a cell sheet because it modulates the rates at which specific polygon classes gain sides due to neighbor cell mitoses. We therefore investigated the implications of cleavage plane bias for the distribution of polygonal cell shapes. We used two distinct computational simulations informed by the empirical division parameters (Figure S2A-C) to model global topology with and without cleavage plane bias (Figures 6 and S5-S6). For both simulation types, the cleavage plane bias values approximated those measured empirically (Figures S5F and S6H). Both an abstract, topological simulator using a Monte-Carlo framework based on topological weights (Figure 6A) (Patel et al., 2009) and a mechanical model of tissue growth based on long-axis divisions (Figure 6D) (Brodland and Veldhuis, 2002) confirmed that cleavage plane bias affects the frequency of hexagonal cells (Figures 6B,E). Moreover, the distribution of mitotic polygonal cells was severely disrupted in the absence of bias, resulting in decreased frequencies of heptagons and increased frequencies of octagons and nonagons (Figures 6C,F). Taken together, these results suggest that cleavage plane bias is required to achieve the normal equilibrium distribution of cell shapes.

DISCUSSION

The results presented here raise several important questions. First, while our analysis provides a geometrical rationale for cleavage plane bias based on

interphase polygon topology (Figure 5), we still cannot rule out the simultaneous action of molecular cues at the cell cortex. In metazoans, epithelial cells often undergo mitosis-induced deformation prior to cleavage (Figures 3C,C'; Figures 4A,A') (Gibson et al., 2006; Thery and Bornens, 2008), and our live imaging results from *Drosophila* strongly suggest that a cellular long axis present in interphase can inform spindle orientation during mitosis (Figure 4). One intriguing possibility is that the interphase distribution of cell-cell contacts determines the localization of cortical cues important for spindle alignment, as has been previously reported (Thery et al., 2007; Thery et al., 2005).

For plant cells, by contrast, our results indicate that local cell packing influences, either directly or indirectly, the placement of the phragmosome and/or pre-prophase band (Pickett-Heaps and Northcote, 1966; Sinnott and Bloch, 1940). There are multiple ways in which this might be accomplished, potentially including stress or strain sensing mechanisms (Hamant et al., 2008; Lintilhac and Vesecky, 1984; Lynch and Lintilhac, 1997), or more simply, based on cytoskeletal mechanisms that are able to sense cell shape (Flanders et al., 1990; Goodbody et al., 1991; Katsuta et al., 1990). To conclude, in addition to our purely geometrical interpretation, our results are also consistent with a hypothesis that in both animals and in plants, local epithelial topology may coordinately specify both the cellular long axis and the distribution of cortical determinants of the eventual cleavage plane.

A second important question concerns the broader implications of cleavage plane bias for the emergence of cell shape. Previous studies of proliferating cell

sheets in *Drosophila* and in *Cucumis* have shown that the distribution of mitotic cell shapes is shifted to have a heptagonal mean, as opposed to the hexagonal mean observed in the population of cells overall (Aegerter-Wilmsen et al., 2010; Gibson et al., 2006; Lewis, 1928). Our simulations (Figures 6A,D) suggest that the mitotic cell distribution is disrupted in the absence of cleavage plane bias (Figures 6C,F), which is consistent with the view that in both *Drosophila* and *Cucumis*, interphase cells passively gain additional sides as a consequence of neighbor cell divisions. This interpretation contrasts with the idea that the mitotic shift solely reflects modulation of the cell cycle by topology-dependent mechanical stress (Aegerter-Wilmsen et al., 2010). Moreover, cleavage plane bias is actually expected to synergize with the mitotic shift. By enriching for super-hexagonal cells in the mitotic cell population, which are entropically favored to neighbor sub-hexagonal cells (Peshkin et al., 1991), the mitotic shift intuitively must amplify the effects of cleavage plane bias.

In summary, by varying the orientation of cell division based on neighbor cell geometry, cells and tissues are able to achieve increased geometric regularity via a dynamic, topology-mediated feedback and control system. Precisely how the default geometric forces that bias cleavage plane orientation interact with other mechanisms of division plane control (Baena-Lopez et al., 2005; Gong et al., 2004; Li et al., 2009; Segalen et al., 2010; Siller et al., 2006; Willemsen et al., 2008) should be an important avenue for future research.

Experimental Procedures:

Fly strains: To visualize the septate junctions, we used a *neuroglian-GFP* exon trap line, which was described in a previous study (Morin et al., 2001). To visualize the chromosomes in parallel, we generated a stock also carrying a Histone-2 RFP marker ((Schuh et al., 2007); Bloomington stock 23650).

Wing disc sample preparation & imaging: Wing discs were dissected from wandering 3rd instar larvae in Ringers' solution, fixed in 4% paraformaldehyde in PBS, and then mounted in 70% glycerol/PBS. For live imaging, discs were carefully dissected and placed in a 50:50 mixture of Ringer's solution (130mM NaCl, 5 mM KCl, 1.5 mM $MgCl_2$), and a second solution (adapted from (Aldaz et al., 2010)), consisting of 2% FBS (Gibco) and 0.5% Pen/Strep (Gibco; 5,000 units/mL penicillin; 5,000 µg/mL streptomycin) in Shields and Sang M3 Insect media (Sigma). Live discs were mounted between two pieces Scotch double-sided tape (3M). Air bubbles were added to the medium using an insulin syringe (BD Ultra-fine with a 30-gauge needle) to potentiate gas exchange. Wing discs were maintained in culture for up to four hours, and imaged at intervals of 15-30 seconds. All samples, live and fixed, were imaged on a Leica SP5 or Leica SP2 confocal microscope with a 63X glycerol or oil objective.

***Cucumis* sample preparation and imaging:** Epidermis was collected from freshly gathered cucumbers approximately 10 cm in length and 2 cm in diameter (Red Ridge Farm, Odessa, MO). Epidermis was peeled in thin layers and fixed in 4% paraformaldehyde in 50 mM KPO_4, 5.0 mM EDTA and 0.2% Tween20 (pH

7) for at least 2 hours at room temperature (adapted from Gallagher and Smith (1999)). Tissue pieces were then washed 2-5 times in dH_2O, and incubated in 5 mg/mL Calcofluor White (Sigma) in PBS for at least 10 minutes before imaging. Images were collected using a Zeiss LSM 510 Meta with a 20x Plan-Apochromat objective, NA 0.8.

Error bars: Unless otherwise specified, error bars refer to a single standard deviation. For the case of ratio distributions, we have reported an average value of the standard deviation. This was computed as follows: the data were randomized and broken into three sub-samples of equal size in order to compute an average value for the standard deviation, based on 1000 random shuffles of the data.

Annotation of *Drosophila* wing disc cytokinetic figures in fixed preparations: A total of 420 cytokinetic figures and their 2946 cellular neighbors were scored by hand, in multiple focal planes to ensure accuracy of topological counts. Out of the 2946 neighbors, 840, or exactly two per cytokinetic figure, were designated as being in the division plane position. Cells were interpreted to be in the division plane position when they occupied the majority of the cytokinetic furrow. Due to the ambiguity of division ordering, cytokinetic figures adjacent to other cytokinetic figures were not considered for analysis.

Annotation of fixed *Drosophila* wing disc epithelial cell sheets: Images of contiguous epithelial regions from *Drosophila* wing disc epithelia were annotated by hand using Microsoft Powerpoint. We used custom-built software to digitize

the annotations for analysis in MATLAB. A total of three such cell sheets, containing 254, 195, and 233 cells, respectively, were analyzed to compute the effective L value (Figure 5C; Table 1), which is described in the text. See Extended Experimental Procedures for additional details.

Live imaging analysis of mitosis in the *Drosophila* wing disc: From live movies, a total of 198 mitotic cells in the *Drosophila* wing disc epithelium were analyzed by hand using ImageJ. With the exception of cells located on compartment boundaries, every scoreable cell on the epithelium was used. To control for possible mechanical influences due to neighboring divisions, we did not consider dividing cells neighboring each other to be scoreable if they rounded up at the same time. Interphase geometry measurements were based on the earliest available time point (the first movie frame), except in rare cases when epithelial morphology obscured the cell in question, in which case a slightly later time point was used. The long axis orientation of each cell was computed using ImageJ, including curvature, based on manual input from the Polygon Selections tool. The identical procedure was used for each cell at later stages, including the eventual cytokinetic figure (see Figure 4A' for an illustration). See the Extended Experimental Procedures for additional details.

Analysis of *Cucumis* epidermal cell sheets:

Images of contiguous regions of *Cucumis* epidermis were annotated by hand using ImageJ. Cell geometry was outlined using the Polygon Selections tool, with one node placed per tri-cellular junction, except in cases of very curved cellular edges, in which additional nodes were used to increase annotation accuracy. To visualize the ellipse of best fit to cell geometry, we used a custom-made ImageJ macro. See the Extended Experimental Procedures for additional information.

Algorithm for computing the minimal energy configuration for local cellular neighborhoods: We used a mechanical relaxation algorithm for cellular networks that has been previously described (Prusinkiewicz and Lindenmayer, 1990). For relaxation (Figure 1), cellular networks were modeled in terms of a balance between edge length tensions (described using ideal springs) and internal pressure (Figure S1). Relaxation was implemented in terms of a system of ordinary differential equations that were solved numerically using the ODE45 solver in MATLAB (Mathworks). See the Extended Experimental Procedures for additional information.

Topological simulations of proliferation: Proliferation was simulated in terms of a network containing exclusively tri-cellular nodes, with wrapping boundary conditions. All division parameters, including division likelihoods of polygonal

cells, the statistical partitioning of mother cell nodes, and the likelihoods of orienting the division plane in the direction of specific polygonal neighbor cell types, are matched to the empirically measured statistics for the *Drosophila* wing disc (see Figure S2A-C). The algorithmic details are described in the Extended Experimental Procedures.

Finite element models of proliferating cell sheets: The FEM simulations (Brodland and Veldhuis, 2002; Chen and Brodland, 2000) model apical contractility, cell-cell adhesion, and all other forces along the cellular edge lengths in terms of a net, interfacial tension, γ, which is generated by rod-like finite elements. Proliferation is modeled in terms of long-axis divisions. Cell-cell rearrangements (T1 transitions) are permitted when cellular edge lengths shrink below a threshold value. See Figure S6 for a comparison between simulations in which T1 transitions are active, versus those for which they are inactive. Additional details are described in the Extended Experimental Procedures.

ACKNOWLEDGEMENTS:

The authors gratefully acknowledge support for this research from the Stowers Institute for Medical Research and the Burroughs Wellcome Fund (to M.C.G.), from the National Science Foundation (to R.N.), from the Natural Sciences and Engineering Research Council of Canada (to G.W.B) and the Howard Hughes Medical Institute (to N.P.). W.T.G. was supported in part by NIH/NIGMS

Molecular Biophysics Training Grant #T32 GM008313 and CTC grant 1029 to MCG.

REFERENCES:

Aegerter-Wilmsen, T., Smith, A.C., Christen, A.J., Aegerter, C.M., Hafen, E., and Basler, K. (2010). Exploring the effects of mechanical feedback on epithelial topology. Development *137*, 499-506.

Aldaz, S., Escudero, L.M., and Freeman, M. (2010). Live imaging of Drosophila imaginal disc development. Proc Natl Acad Sci U S A *107*, 14217-14222.

Baena-Lopez, L.A., Baonza, A., and Garcia-Bellido, A. (2005). The orientation of cell divisions determines the shape of Drosophila organs. Curr Biol *15*, 1640-1644.

Black, S.D., and Vincent, J.P. (1988). The first cleavage plane and the embryonic axis are determined by separate mechanisms in Xenopus laevis. II. Experimental dissociation by lateral compression of the egg. Dev Biol *128*, 65-71.

Brodland, G.W., and Veldhuis, J.H. (2002). Computer simulations of mitosis and interdependencies between mitosis orientation, cell shape and epithelia reshaping. J Biomech *35*, 673-681.

Buschmann, H., Chan, J., Sanchez-Pulido, L., Andrade-Navarro, M.A., Doonan, J.H., and Lloyd, C.W. (2006). Microtubule-associated AIR9 recognizes the cortical division site at preprophase and cell-plate insertion. Curr Biol *16*, 1938-1943.

Chen, H.H., and Brodland, G.W. (2000). Cell-level finite element studies of viscous cells in planar aggregates. J Biomech Eng *122*, 394-401.

Cowan, R., and Morris, V.B. (1988). Division rules for polygonal cells. J Theor Biol *131*, 33-42.

Dubertret, B., Aste, T., Ohlenbusch, H.M., and Rivier, N. (1998). Two-dimensional froths and the dynamics of biological tissues. Physical Review E *58*, 6368–6378

Dubertret, B., and Rivier, N. (1997). The renewal of the epidermis: a topological mechanism. Biophys J *73*, 38-44.

Fernandez-Minan, A., Martin-Bermudo, M.D., and Gonzalez-Reyes, A. (2007). Integrin signaling regulates spindle orientation in Drosophila to preserve the follicular-epithelium monolayer. Curr Biol *17*, 683-688.

Fischer, E., Legue, E., Doyen, A., Nato, F., Nicolas, J.F., Torres, V., Yaniv, M., and Pontoglio, M. (2006). Defective planar cell polarity in polycystic kidney disease. Nat Genet *38*, 21-23.

Flanders, D.J., Rawlins, D.J., Shaw, P.J., and Lloyd, C.W. (1990). Nucleus-associated microtubules help determine the division plane of plant epidermal cells: avoidance of four-way junctions and the role of cell geometry. J Cell Biol *110*, 1111-1122.

Gallagher, K., and Smith, L.G. (1999). discordia mutations specifically misorient asymmetric cell divisions during development of the maize leaf epidermis. Development *126*, 4623-4633.

Gibson, M.C., Patel, A.B., Nagpal, R., and Perrimon, N. (2006). The emergence of geometric order in proliferating metazoan epithelia. Nature *442*, 1038-1041.

Gong, Y., Mo, C., and Fraser, S.E. (2004). Planar cell polarity signalling controls cell division orientation during zebrafish gastrulation. Nature *430*, 689-693.

Goodbody, K.C., Venverloo, C.J., and Lloyd, C.W. (1991). Laser Microsurgery Demonstrates That Cytoplasmic Strands Anchoring the Nucleus across the Vacuole of Premitotic Plant-Cells Are under Tension - Implications for Division Plane Alignment. Development *113*, 931-939.

Gray, D., Plusa, B., Piotrowska, K., Na, J., Tom, B., Glover, D.M., and Zernicka-Goetz, M. (2004). First cleavage of the mouse embryo responds to change in egg shape at fertilization. Curr Biol *14*, 397-405.

Hamant, O., Heisler, M.G., Jonsson, H., Krupinski, P., Uyttewaal, M., Bokov, P., Corson, F., Sahlin, P., Boudaoud, A., Meyerowitz, E.M.*, et al.* (2008). Developmental patterning by mechanical signals in Arabidopsis. Science *322*, 1650-1655.

Hofmeister, W. (1863). Zusatze und Berichtigungen zu den 1851 veröffentlichen Untersuchungengen der Entwicklung höherer Kryptogamen. Jahrbucher für Wissenschaft und Botanik *3*, 259-293.

Johnston, C.A., Hirono, K., Prehoda, K.E., and Doe, C.Q. (2009). Identification of an Aurora-A/PinsLINKER/Dlg spindle orientation pathway using induced cell polarity in S2 cells. Cell *138*, 1150-1163.
Katsuta, J., Hashiguchi, Y., and Shibaoka, H. (1990). The Role of the Cytoskeleton in Positioning of the Nucleus in Premitotic Tobacco by-2 Cells. J Cell Sci *95*, 413-422.
Korn, R.W., and Spalding, R.M. (1973). The Geometry of Plant Epidermal Cells. New Phytologist *72*, 1357-1365.
Kost, B., and Chua, N.H. (2002). The plant cytoskeleton: Vacuoles and cell walls make the difference. Cell *108*, 9-12.
Lewis, F.T. (1928). The Correlation Between Cell Division and the Shapes and Sizes of Prismatic Cells in the Epidermis of Cucumis. The Anatomical Record *38*, 341-376.
Li, W., Kale, A., and Baker, N.E. (2009). Oriented cell division as a response to cell death and cell competition. Curr Biol *19*, 1821-1826.
Lintilhac, P.M., and Vesecky, T.B. (1984). Stress-induced alignment of division plane in plant tissues grown *in vitro*. Nature *307*, 363-364.
Lloyd, C.W. (1991). How Does the Cytoskeleton Read the Laws of Geometry in Aligning the Division Plane of Plant-Cells. Development, 55-65.
Lynch, T.M., and Lintilhac, P.M. (1997). Mechanical signals in plant development: a new method for single cell studies. Dev Biol *181*, 246-256.
Miri, M., and Rivier, N. (2006). Universality in two-dimensional cellular structures evolving by cell division and disappearance. Phys Rev E Stat Nonlin Soft Matter Phys *73*, 031101.
Morin, X., Daneman, R., Zavortink, M., and Chia, W. (2001). A protein trap strategy to detect GFP-tagged proteins expressed from their endogenous loci in Drosophila. Proc Natl Acad Sci U S A *98*, 15050-15055.
O'Connell, C.B., and Wang, Y.L. (2000). Mammalian spindle orientation and position respond to changes in cell shape in a dynein-dependent fashion. Mol Biol Cell *11*, 1765-1774.
Palevitz, B.A. (1987). Actin in the Preprophase Band of Allium-Cepa. J Cell Biol *104*, 1515-1519.
Patel, A.B., Gibson, W.T., Gibson, M.C., and Nagpal, R. (2009). Modeling and inferring cleavage patterns in proliferating epithelia. PLoS Comput Biol *5*, e1000412.
Peshkin, M.A., Strandburg, K.J., and Rivier, N. (1991). Entropic predictions for cellular networks. Phys Rev Lett *67*, 1803-1806.
Pickett-Heaps, J.D., and Northcote, D.H. (1966). Organization of microtubules and endoplasmic reticulum during mitosis and cytokinesis in wheat meristems. J Cell Sci *1*, 109-120.
Prusinkiewicz, P., and Lindenmayer, A. (1990). The Algorithmic Beauty of Plants (New York, Springer-Verlag).
Quyn, A.J., Appleton, P.L., Carey, F.A., Steele, R.J., Barker, N., Clevers, H., Ridgway, R.A., Sansom, O.J., and Nathke, I.S. (2010). Spindle orientation bias in gut epithelial stem cell compartments is lost in precancerous tissue. Cell Stem Cell *6*, 175-181.
Rivier, N., and Lissowski, A. (1982). On the correlation between sizes and shapes of cells in epithelial mosaics. J Phys A: Math Gen *15*, L143-L148.
Rivier, N., Schliecker, G., and Dubertret, B. (1995). The stationary state of epithelia. Acta Biotheoretica *43*, 403-423.
Saburi, S., Hester, I., Fischer, E., Pontoglio, M., Eremina, V., Gessler, M., Quaggin, S.E., Harrison, R., Mount, R., and McNeill, H. (2008). Loss of Fat4 disrupts PCP signaling and oriented cell division and leads to cystic kidney disease. Nat Genet *40*, 1010-1015.
Schuh, M., Lehner, C.F., and Heidmann, S. (2007). Incorporation of Drosophila CID/CENP-A and CENP-C into centromeres during early embryonic anaphase. Curr Biol *17*, 237-243.

Segalen, M., Johnston, C.A., Martin, C.A., Dumortier, J.G., Prehoda, K.E., David, N.B., Doe, C.Q., and Bellaiche, Y. (2010). The Fz-Dsh planar cell polarity pathway induces oriented cell division via Mud/NuMA in Drosophila and zebrafish. Dev Cell *19*, 740-752.
Siller, K.H., Cabernard, C., and Doe, C.Q. (2006). The NuMA-related Mud protein binds Pins and regulates spindle orientation in Drosophila neuroblasts. Nat Cell Biol *8*, 594-600.
Siller, K.H., and Doe, C.Q. (2009). Spindle orientation during asymmetric cell division. Nat Cell Biol *11*, 365-374.
Sinnott, E.W., and Bloch, R. (1940). Cytoplasmic behavior during division of vacuolate plant cells. P Natl Acad Sci USA *26*, 223-227.
Speicher, S., Fischer, A., Knoblich, J., and Carmena, A. (2008). The PDZ protein Canoe regulates the asymmetric division of Drosophila neuroblasts and muscle progenitors. Curr Biol *18*, 831-837.
Strauss, B., Adams, R.J., and Papalopulu, N. (2006). A default mechanism of spindle orientation based on cell shape is sufficient to generate cell fate diversity in polarised Xenopus blastomeres. Development *133*, 3883-3893.
Thery, M., and Bornens, M. (2008). Get round and stiff for mitosis. HFSP J *2*, 65-71.
Thery, M., Jimenez-Dalmaroni, A., Racine, V., Bornens, M., and Julicher, F. (2007). Experimental and theoretical study of mitotic spindle orientation. Nature *447*, 493-496.
Thery, M., Racine, V., Pepin, A., Piel, M., Chen, Y., Sibarita, J.B., and Bornens, M. (2005). The extracellular matrix guides the orientation of the cell division axis. Nat Cell Biol *7*, 947-953.
Traas, J., Bellini, C., Nacry, P., Kronenberger, J., Bouchez, D., and Caboche, M. (1995). Normal Differentiation Patterns in Plants Lacking Microtubular Preprophase Bands. Nature *375*, 676-677.
Vanstraelen, M., Van Damme, D., De Rycke, R., Mylle, E., Inze, D., and Geelen, D. (2006). Cell cycle-dependent targeting of a kinesin at the plasma membrane demarcates the division site in plant cells. Current Biology *16*, 308-314.
Walker, K.L., Muller, S., Moss, D., Ehrhardt, D.W., and Smith, L.G. (2007). Arabidopsis TANGLED identifies the division plane throughout mitosis and cytokinesis. Curr Biol *17*, 1827-1836.
Willemsen, V., Bauch, M., Bennett, T., Campilho, A., Wolkenfelt, H., Xu, J., Haseloff, J., and Scheres, B. (2008). The NAC domain transcription factors FEZ and SOMBRERO control the orientation of cell division plane in Arabidopsis root stem cells. Dev Cell *15*, 913-922.
Wright, A.J., Gallagher, K., and Smith, L.G. (2009). discordia1 and alternative discordia1 function redundantly at the cortical division site to promote preprophase band formation and orient division planes in maize. Plant Cell *21*, 234-247.

Figure legends:

Figure 1: Local epithelial topology is predicted to influence the geometry of an epithelial cell.

(A) A stereotypical simple columnar epithelium. Black spots represent nuclei. **(B)** The *Drosophila* wing disc epithelium, with *nrg*-GFP (*green*) marking the septate junctions. **(B')** A planar network representation of (B). **(C)** A model for finding the minimum energy configuration of cell packing, based on internal pressure and ideal springs. **(D-F)** (*Initial states, left*) Initial conditions for the relaxation algorithm. Each case varies the topology of the marked cell. (*Relaxed states, right*) At equilibrium, cell shape is specified by a balance between pressure and tension. The central cell's shape is strongly influenced by the labeled cell's topology. See also Figure S1.

Figure 2: The orientation of a cell's short axis is predicted to correlate with its quadrilateral and pentagonal neighbors, and to anti-correlate with heptagonal and octagonal neighbors.

(A) Neighbor cell topology, N, influences the direction of the cellular long axis (*solid line*) and short axis (*dashed line*), based on an ellipse of best-fit (*red*). Second order and higher neighbors, which are uniformly hexagonal, are not shown. For N< 6, the short axis is oriented towards N-sided cell *N*; for N>6, it is oriented perpendicular to *N*. **(B)** The attraction of the short axis to quadrilateral cells (N=4) is robust to heterogeneity in the local cell neighborhood. **(C)** We computed the cleavage plane index, or fraction of neighbors in each polygon class (*black line*) located adjacent to the central cell's short axis (presumed cleavage plane). Neighbor cells having N<6 are significantly enriched in this position. Conversely, neighbors having N >6 are under-represented. For comparison, for a randomly oriented division plane, all N values occur with similar frequency (*green*), which is close to the null hypothesis of 2/7 (*red*). **(D)** We defined an acute angle, θ, with respect to a cell's short axis (*dashed red line*), as well as the neighbor topology in direction θ (*green cells*). **(E)** On average, neighbor topology (*black*) is an increasing function of acute angle θ. Error bars represent the standard deviation in the sample mean topology in direction θ per cell (an average of the 4 positions on the cell cortex corresponding to the θ, over 420 such cells).

Figure 3: In both plants and animals, a dividing cell's cleavage plane correlates with its quadrilateral and pentagonal neighbors, and anti-correlates with heptagonal and octagonal neighbors.

(A) The *Drosophila* wing imaginal disc, stained with anti-DLG to mark the junctions (*green*) and anti-PH3 to mark chromatin (*blue*). **(B-D; B'-D'),** Cell division proceeds in the plane of the epithelium via a stereotyped division process including interphase (I), mitosis (M), and cytokinesis (C). Actin staining is shown in red. **(E)** We can infer the topological complement of neighbors, as well as the division orientation of dividing cells, from cytokinetic figures. Junctions are marked by a *nrg*-GFP protein trap (*red*). **(F-G)** We examined > 400 such figures, and sorted the neighbors by polygon class. The neighbors on the division plane (*red*) are a subset of the full complement of neighbors (*green and red*). **(H)** An overlay of the predicted mitotic cleavage plane bias based on our mechanical model (*black*), with the biases computed from both *Drosophila* wing disc epithelium (*blue*) and cucumber epidermis (*red*). Each is compared with the topological null hypothesis (*green*). See also Figure S2 for further information.

Figure 4: *Drosophila* wing disc cells approximately obey a long-axis division rule.

(A) Time series analysis illustrates the process in which an interphase cell entering mitosis gradually dilates before reaching full rounding, and then subsequently undergoes cytokinesis, in an orientation approximately predicted by its interphase long axis. (A') Drawings of the process described in the corresponding panels in A, including the mitotic cell and its immediate neighbors. The long axis of the ellipse of best fit (*red*) is labeled with a solid line, whereas the dashed line (predicted cleavage plane) represents the short axis. **(B)** The eventual orientation of the cleavage plane can be predicted based on the interphase long axis orientation. The red line (zero deviation from long-axis division) represents a perfect correlation between the interphase long axis and the long axis of the resulting cytokinetic figure. Blue bars show the number of cells (represented by radial distance from the center) that divided with a particular angular deviation from the interphase long axis. On average, the deviation was approximately 27.1 degrees. The data is represented by the first quadrant (0˚ to 90˚), which is also displayed symmetrically in the other three quadrants (90˚ to 360˚). **(C)** The bias curve prediction that incorporates the measured deviation of 27 degrees from the long axis (*red*) is significantly closer to the empirically measured cleavage plane bias (*blue*) than the naïve long-axis prediction is (*black*). A Gaussian noise model with 27 degree standard deviation

gives a similar result (data not shown). We controlled for the influence of topological relationships by using the same local neighborhoods as were measured from the empirical data (*blue*). See also the Extended Experimental Procedures and Figure S3, which suggests a long axis mechanism may also operate in *Cucumis*.

Figure 5: Fundamental packing constraints are sufficient to explain cleavage plane bias.

(A) Hexagons pack at 120-degree angles. **(B)** A 4-sided cell distorts the internal angles of the surrounding hexagons, inducing a long axis. **(C)** A geometrical argument for division plane bias. The N-sided neighbor cell influences the ratio of the horizontal axis, d_m to the vertical axis, h_m, in the *M*-cell. When d_m:h_m > 1, the N cell is in the predicted cleavage plane position for the *M*-cell. **(D)** A plot of the ratio d_m:h_m, for different values of N and L. Above the gray line, the N-cell is in the *M*-cell's predicted division plane; the opposite is true below the gray line. **(E-F)** Both N and L influence the direction of the long axis in the *M* cell. **(E)** The value of N influences the direction of the long axis in the *M* cell (top cell), for constant L. **(F)** The long axis of the M-cell is influenced by the side length, L, for a constant N-value. See also Figure S4.

Figure 6: Cleavage plane bias participates in cell shape emergence, and is required for wild-type cell packing.

(A) The topological simulator does not model cellular mechanics, but does explicitly keep track of topological neighbor relationships. Based on topological weights, division likelihood, division symmetry, and cleavage plane bias are matched to empirically measured statistics in a Monte-Carlo framework (see Figures S2A-C). **(B)** Hexagonal frequency declines by approximately 4% in the absence of bias. Arrows highlight this difference. **(C)** The distribution of mitotic cells shows pronounced alterations in the absence of bias. Arrows highlight the differences. **(D)** The finite element simulator models cellular mechanics, division, and rearrangement. The simulator captures mechanics in terms of a net, interfacial tension, which is modeled using rod-like finite elements. Division likelihoods are informed by the empirically measured values (Figure S2A). Cleavage plane bias approximates the empirical values, and is achieved using long-axis divisions. For finite element simulations incorporating cellular rearrangements (T1 transitions), see Figure S6. **(E)** In the absence of bias, hexagonal frequency declines by about 4% (compare with panel B). **(F)** The

distribution of mitotic cells again shows pronounced alterations (compare with panel C). See also Figures S5-S6.

Table 1: *The effective L value changes by approximately 40% in wild type Drosophila tissues.*

N-cell polygon class	Average effective L Value	Standard deviation in effective L Value	Sample size (hexagonal interfaces with N-cells)
4	1.2504	.4165	22 interfaces
5	1.1158	.4141	231 interfaces
6	1.0580	.4053	487 interfaces
7	.9237	.4081	341 interfaces
8	.9620	.5405	46 interfaces

Table 1 legend: For each value of N (column 1), the average effective L value has been computed (column 2), as well as the sample standard deviation (column 3), using empirically extracted cellular networks from the *Drosophila* wing imaginal disc (Extended Experimental Procedures). The sample size for each calculation is given in column 4. The effective L value, computed for hexagonal cells, is the average value of an edge shared with an N-sided neighbor, divided by the average length of the remaining 5 edges.

Figure
Figure 1:
Click here to download Figure: Gibson_cellms_Figure1.pdf

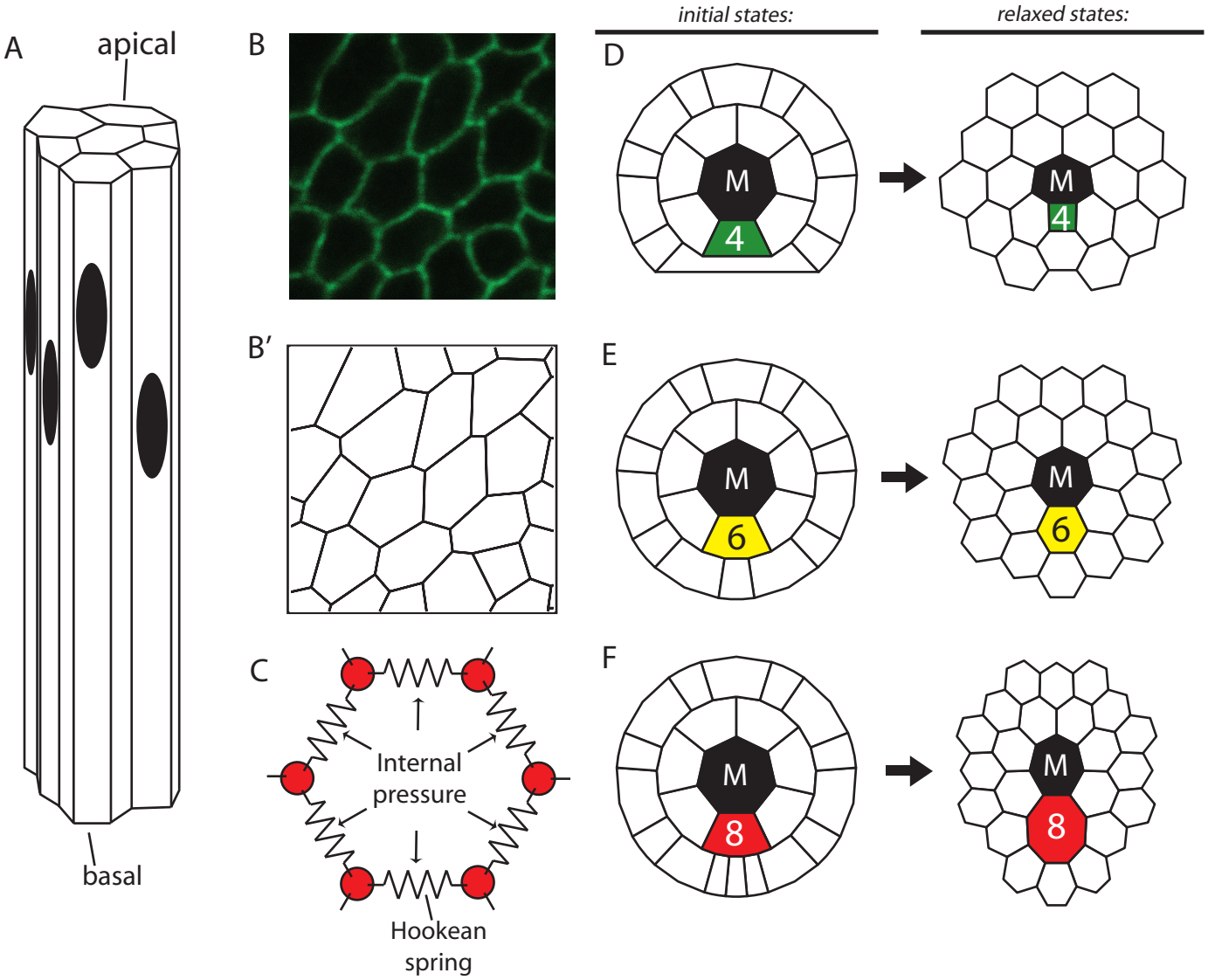

Figure

Click here to download Figure: Gibson_cellms_Figure2.pdf

Figure 2:

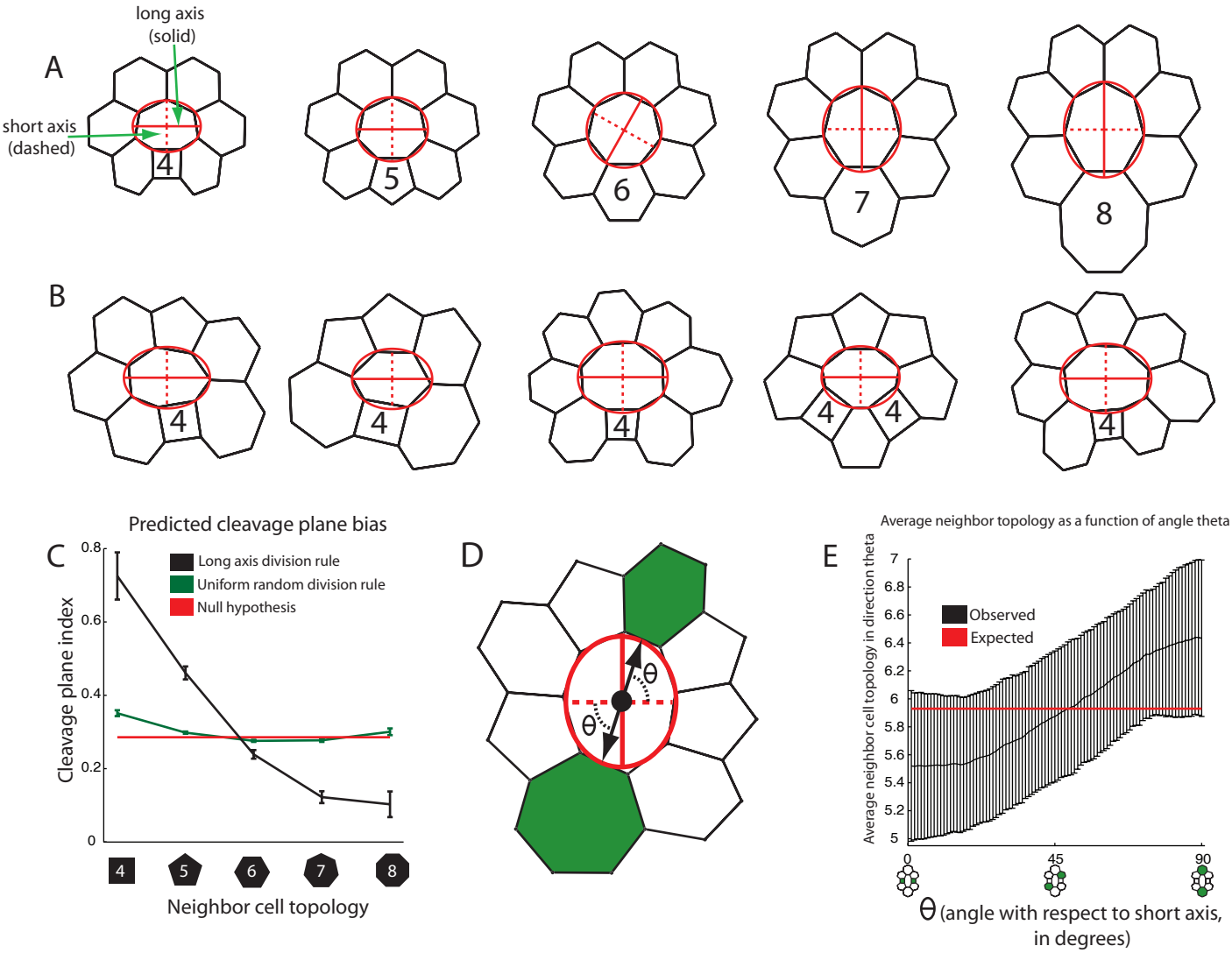

Figure
Click here to download Figure: Gibson_cellms_Figure3.pdf

Figure 3:

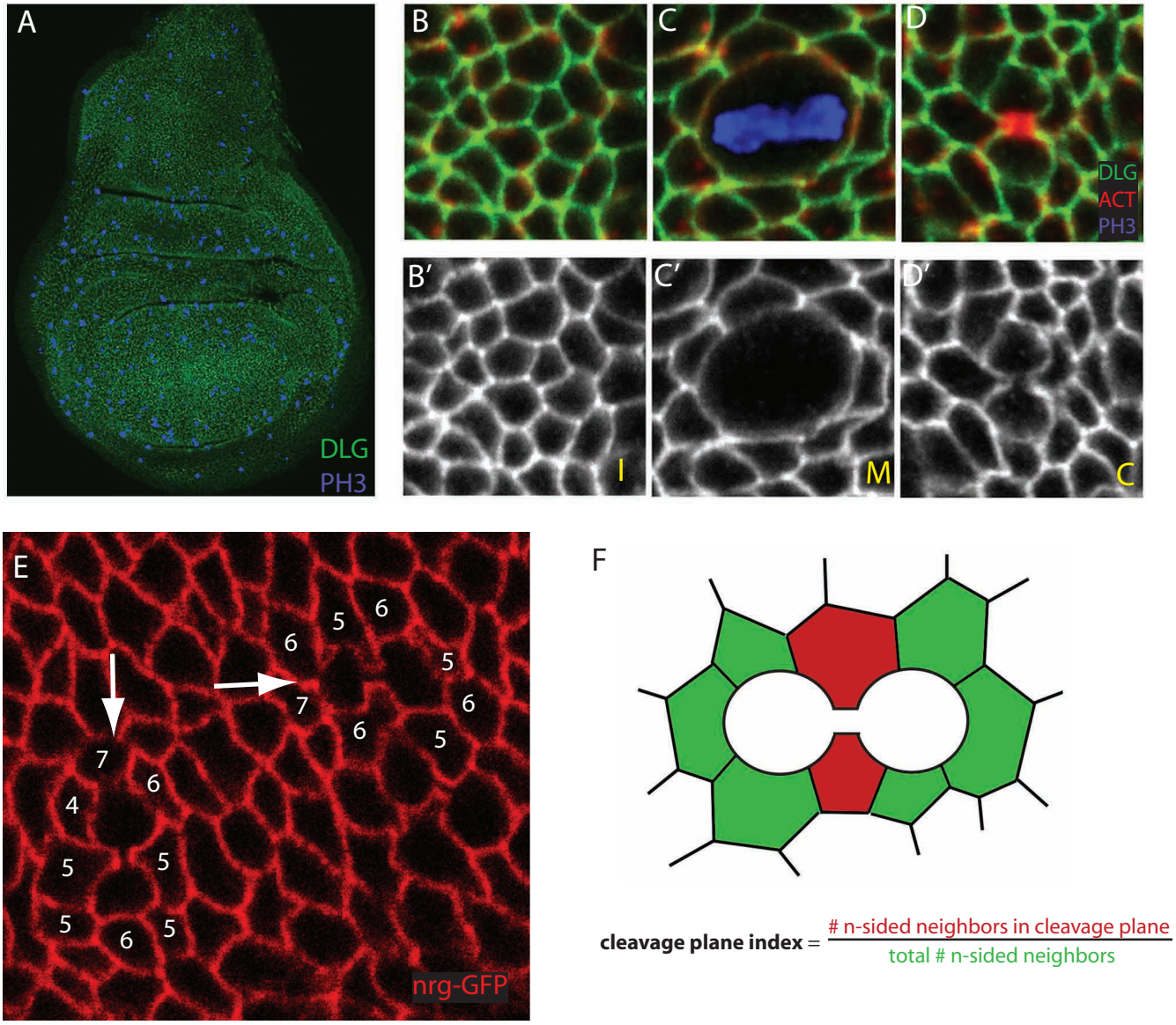

Figure
Figure 4:
Click here to download Figure: Gibson_cellms_Figure4.pdf

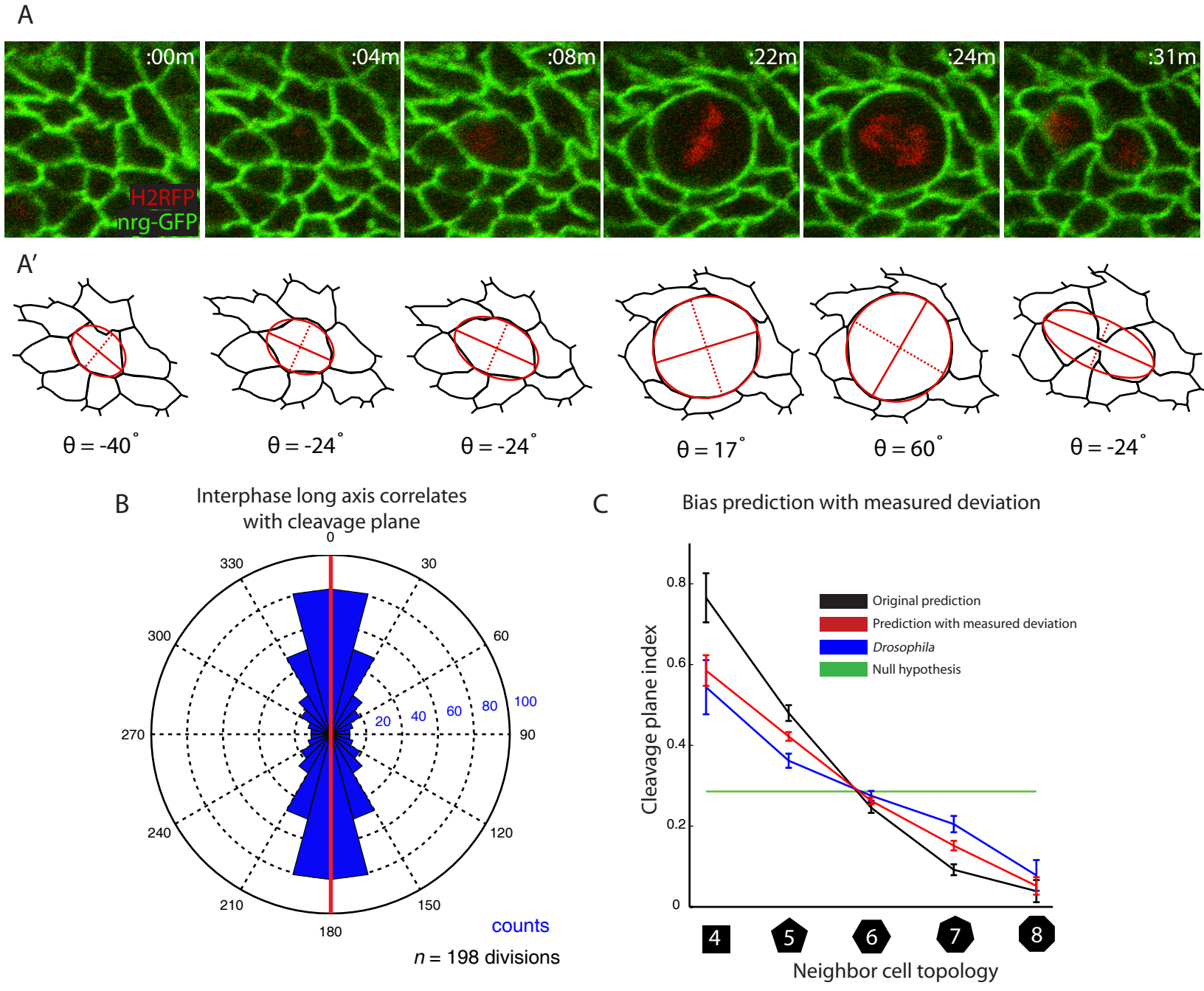

Figure

Click here to download Figure: Gibson_cellms_Figure5.pdf

Figure 5:

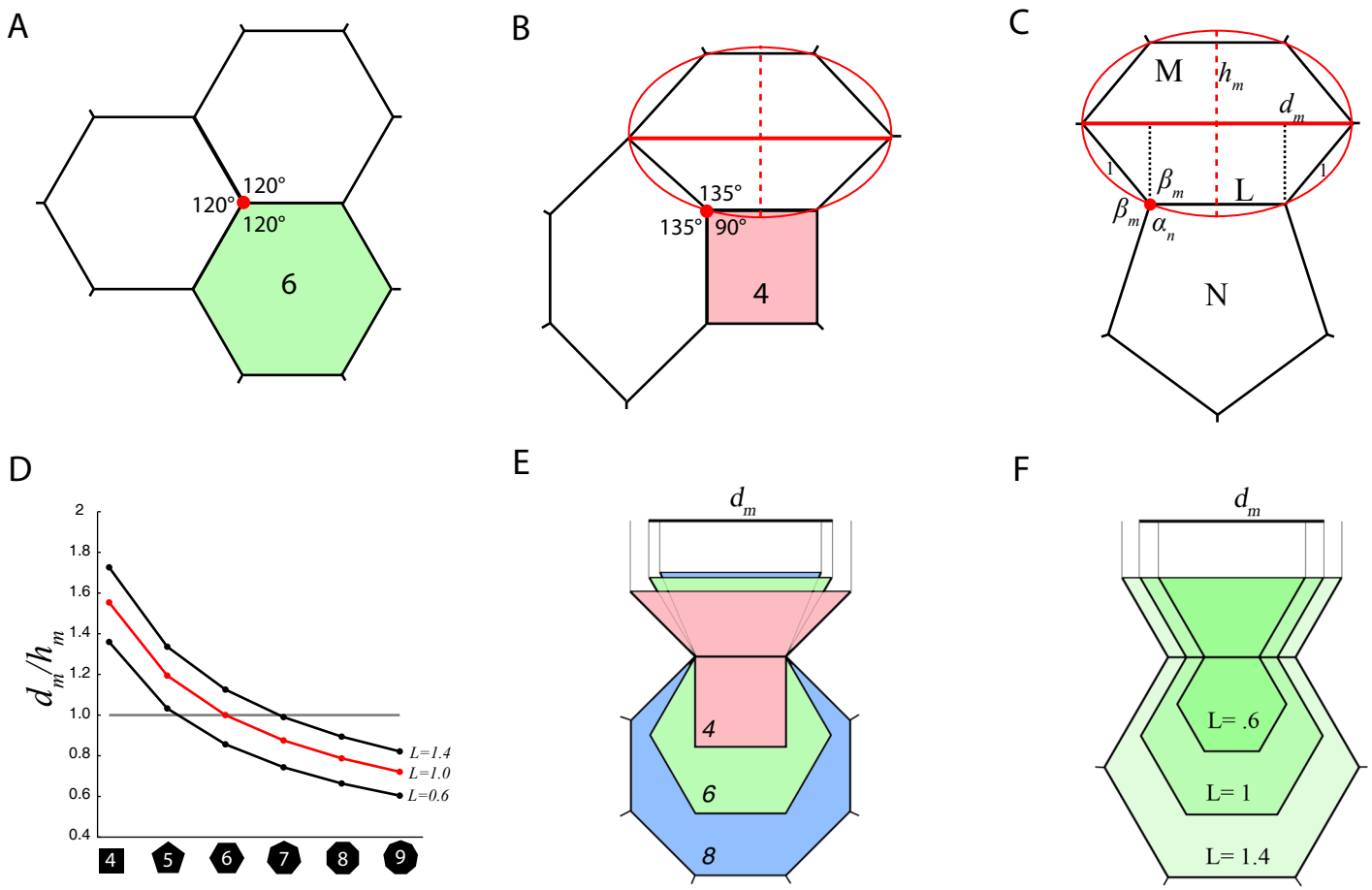

Figure
Click here to download Figure: Gibson_cellms_Figure6.pdf

Figure 6:

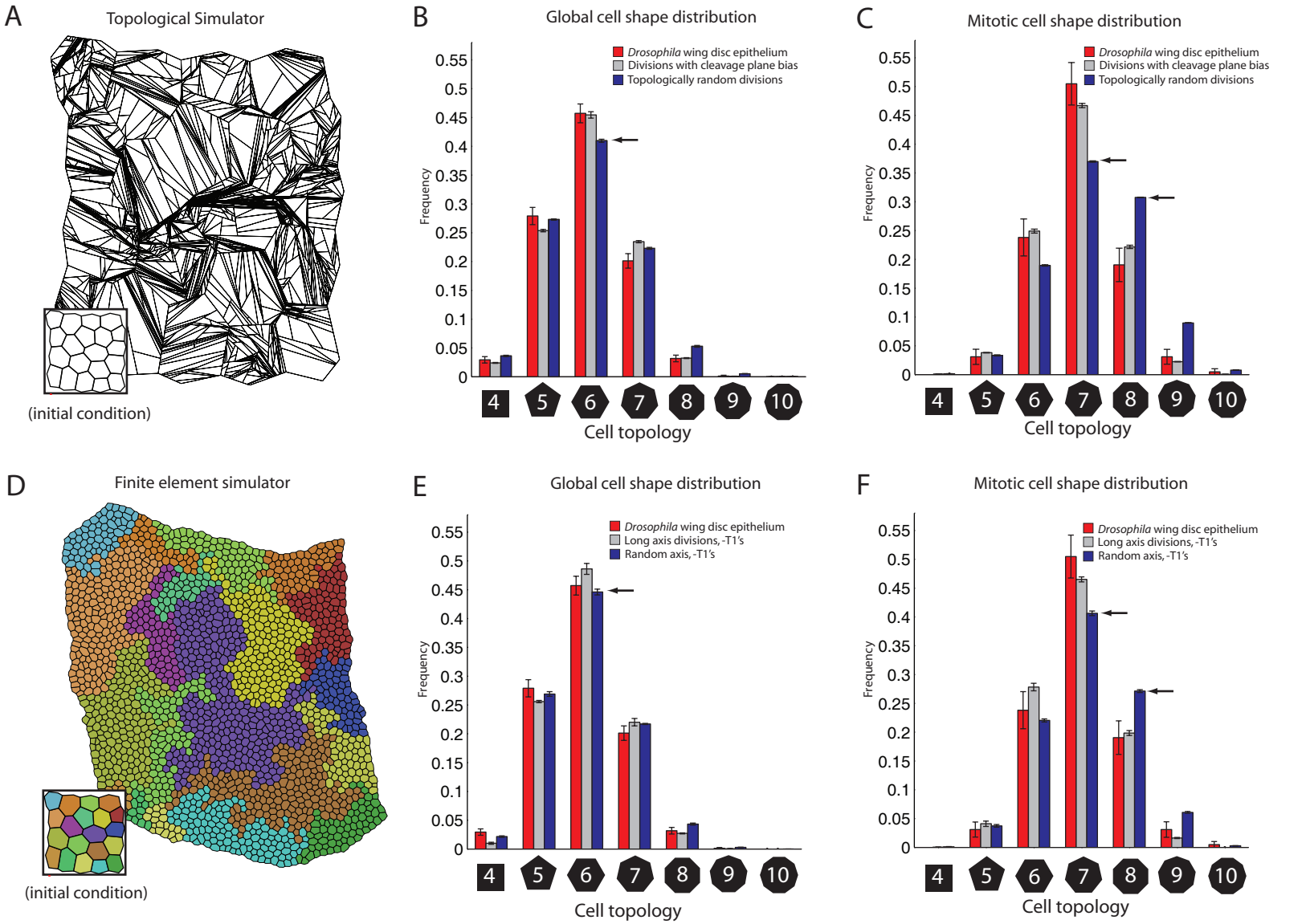

Supplemental material for "Control of the mitotic cleavage plane by local epithelial topology"

WT Gibson, JH Veldhuis, B Rubinstein, HN Cartwright, N Perrimon, GW Brodland, R Nagpal, & MC Gibson*

*Contact: <mg2@stowers.org>

Inventory for supplemental material:

Supplemental material for "Control of the mitotic cleavage plane by local epithelial topology"

WT Gibson, JH Veldhuis, B Rubinstein, HN Cartwright, N Perrimon, GW Brodland, R Nagpal, & MC Gibson*

*Contact: <mg2@stowers.org>

Inventory for supplemental material:

I. Supplemental data

Figure S1:

A Diagram for relaxation algorithm

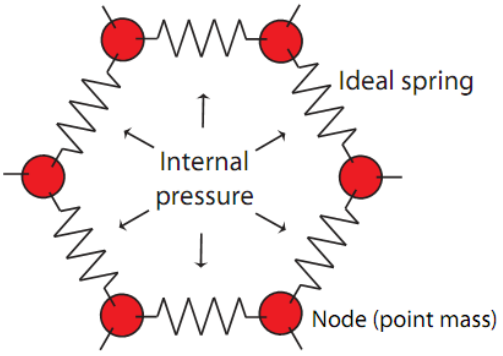

B Structural legend

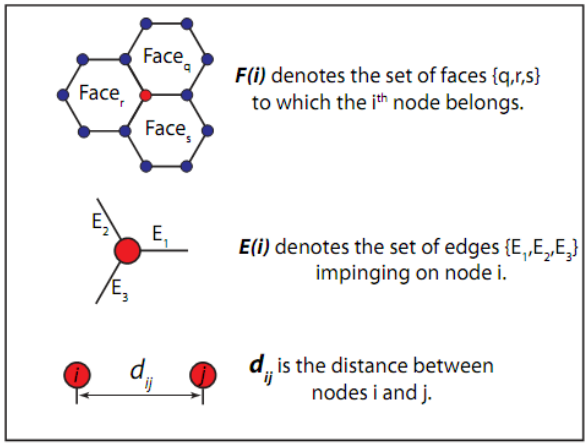

C Outline of algorithmic terms

(1) Node i **feels a tensional force** T_{ij} when the distance d_{ij} between nodes i and j exceeds l_0, the spring's rest length.

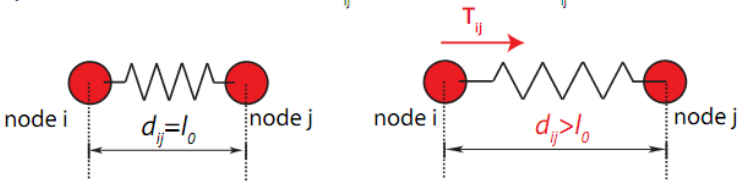

$$\|T_{ij}\| \propto (d_{ij} - l_0)$$

(2) Nodes i and j **feel a force of expansion** $P_{ij}(k)$ **due to internal pressure** from within face k.

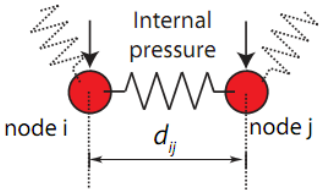

$$\|P_{ij}(k)\| \propto \frac{d_{ij}}{A_k}$$

(A_k is the area of face k).

(3) A frictional force opposes the motion of node i, and is proportional to node i's velocity.

$$\|Force_{friction}\| = vC_i$$

(C_i is the friction coefficient for node i).

D. Equation used to compute the equilibrium configuration

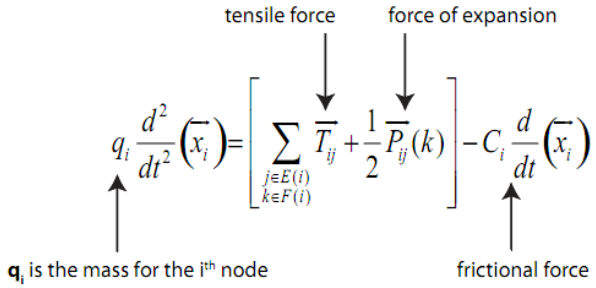

Figure S2:

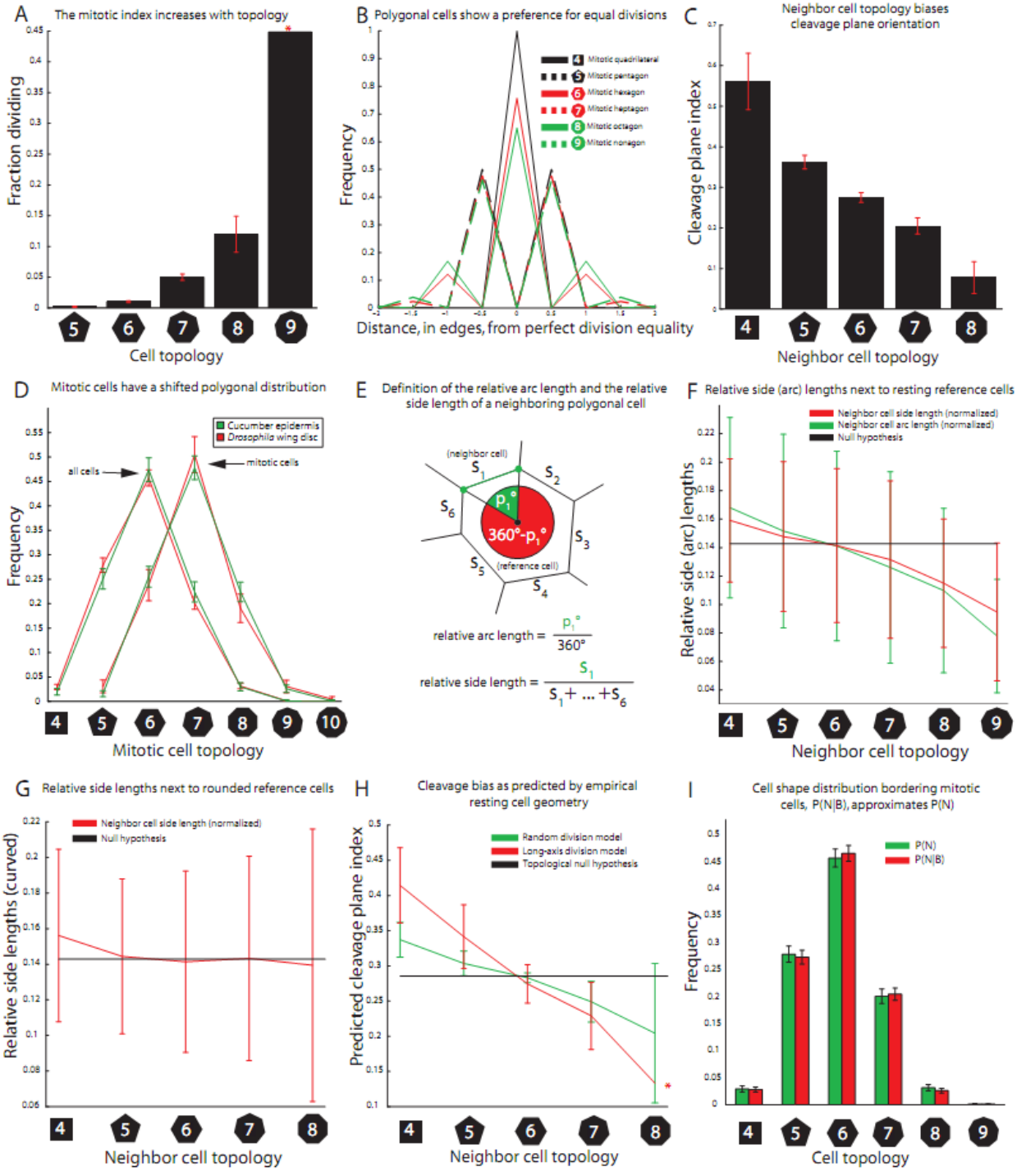
A
The mitotic index increases with topology
Fraction dividing
Cell topology
B
Polygonal cells show a preference for equal divisions
Frequency
Mitotic quadrilateral
Mitotic pentagon
Mitotic hexagon
Mitotic heptagon
Mitotic octagon
Mitotic nonagon
Distance, in edges, from perfect division equality
C
Neighbor cell topology biases cleavage plane orientation
Cleavage plane index
Neighbor cell topology
D
Mitotic cells have a shifted polygonal distribution
Cucumber epidermis
Drosophila wing disc
all cells
mitotic cells
Frequency
Mitotic cell topology
E
Definition of the relative arc length and the relative side length of a neighboring polygonal cell
(neighbor cell)
(reference cell)
relative arc length = p1°/360°
relative side length = S1/(S1+ ... +S6)
F
Relative side (arc) lengths next to resting reference cells
Neighbor cell side length (normalized)
Neighbor cell arc length (normalized)
Null hypothesis
Relative side (arc) lengths
Neighbor cell topology
G
Relative side lengths next to rounded reference cells
Neighbor cell side length (normalized)
Null hypothesis
Relative side lengths (curved)
Neighbor cell topology
H
Cleavage bias as predicted by empirical resting cell geometry
Random division model
Long-axis division model
Topological null hypothesis
Predicted cleavage plane index
Neighbor cell topology
I
Cell shape distribution bordering mitotic cells, P(N|B), approximates P(N)
P(N)
P(N|B)
Frequency
Cell topology

Figure S3:

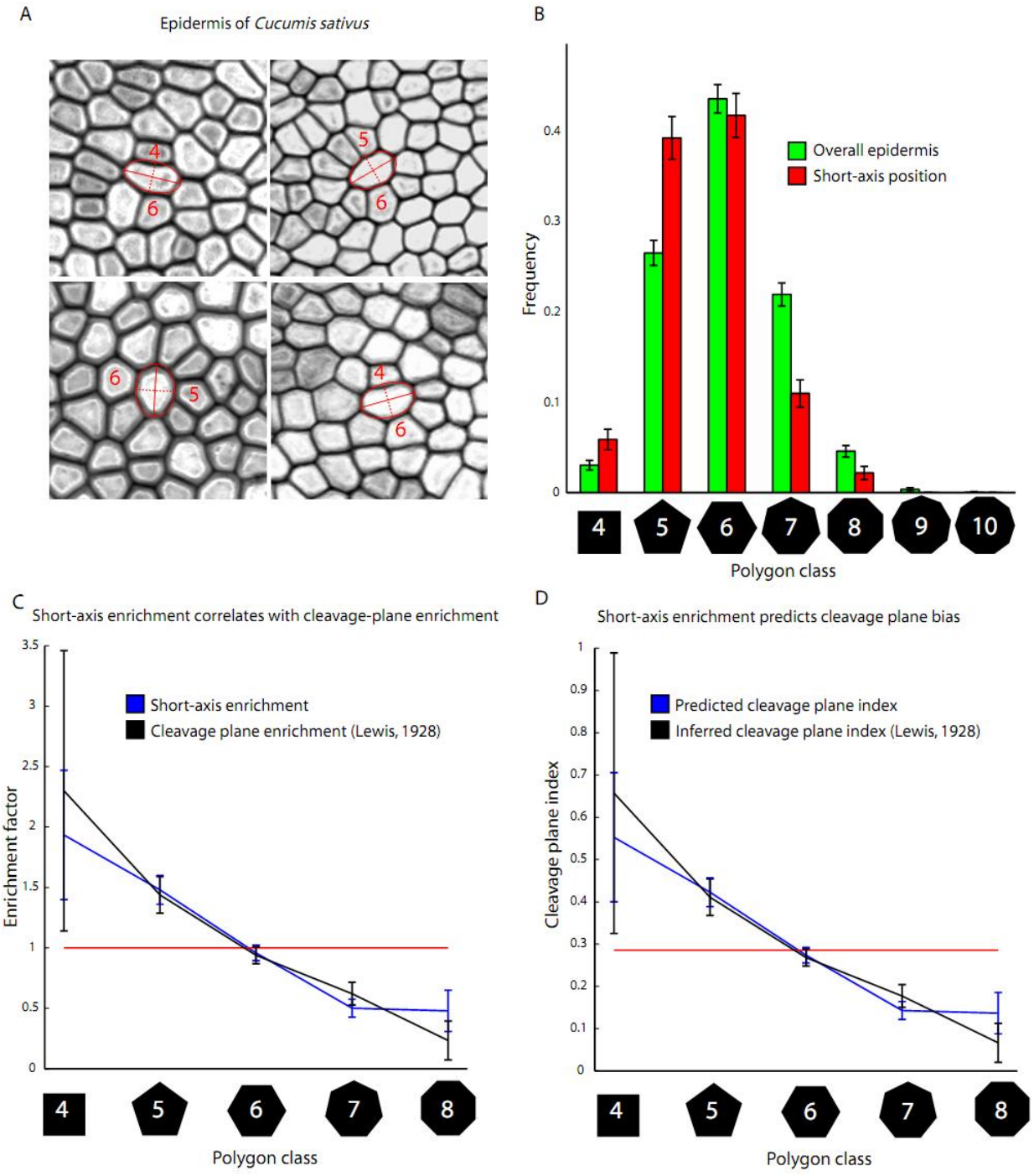
A
Epidermis of *Cucumis sativus*
4
6
5
6
6
5
4
6
B
Frequency
0
0.1
0.2
0.3
0.4
Overall epidermis
Short-axis position
4
5
6
7
8
9
10
Polygon class
C
Short-axis enrichment correlates with cleavage-plane enrichment
Enrichment factor
0
0.5
1
1.5
2
2.5
3
3.5
Short-axis enrichment
Cleavage plane enrichment (Lewis, 1928)
4
5
6
7
8
Polygon class
D
Short-axis enrichment predicts cleavage plane bias
Cleavage plane index
0
0.1
0.2
0.3
0.4
0.5
0.6
0.7
0.8
0.9
1
Predicted cleavage plane index
Inferred cleavage plane index (Lewis, 1928)
4
5
6
7
8
Polygon class

Figure S4:

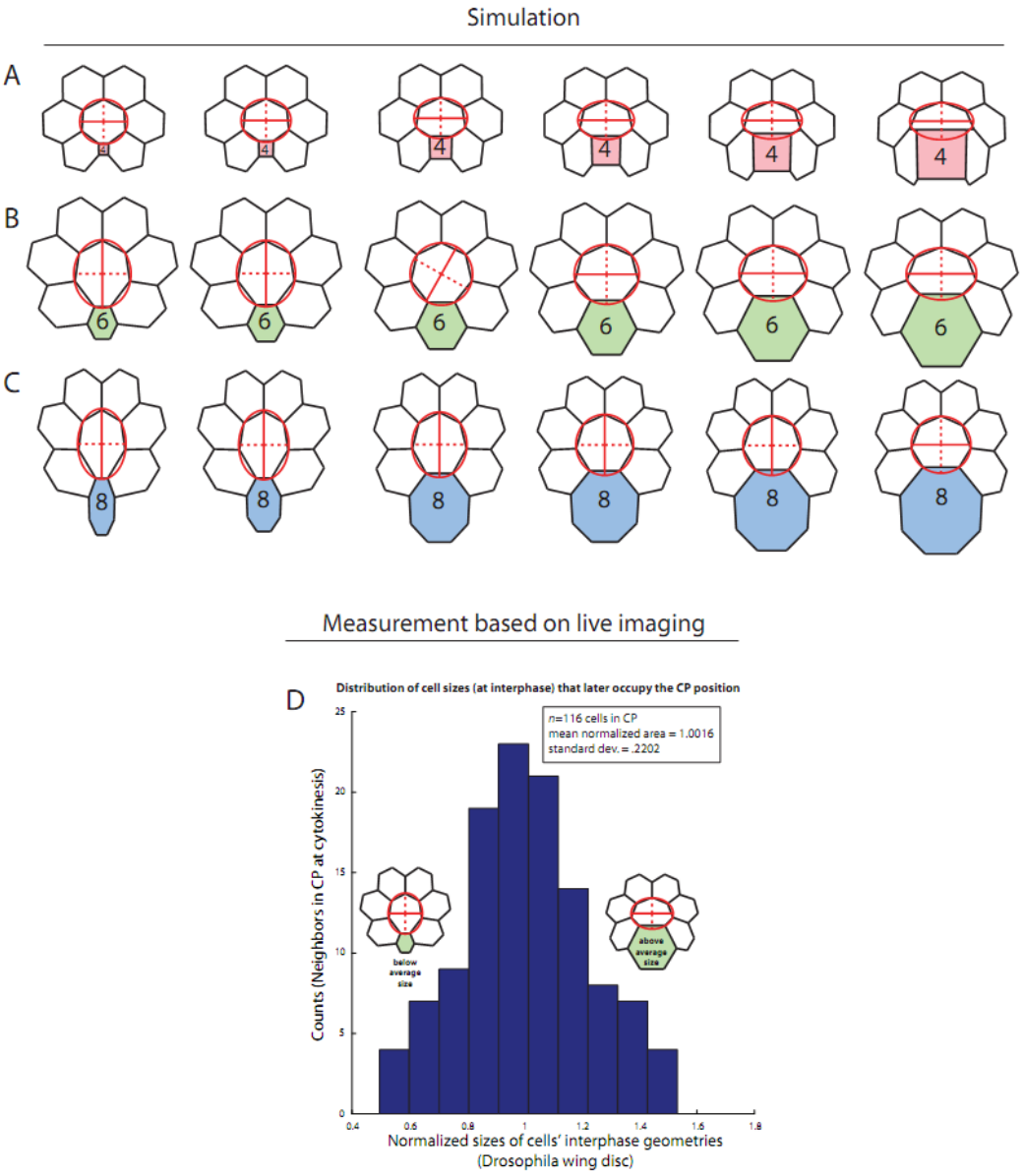
Simulation
A
4
B
6
C
8
Measurement based on live imaging
D
Distribution of cell sizes (at interphase) that later occupy the CP position
n=116 cells in CP
mean normalized area = 1.0016
standard dev. = .2202
Counts (Neighbors in CP at cytokinesis)
below average size
above average size
Normalized sizes of cells' interphase geometries
(Drosophila wing disc)

Figure S5:

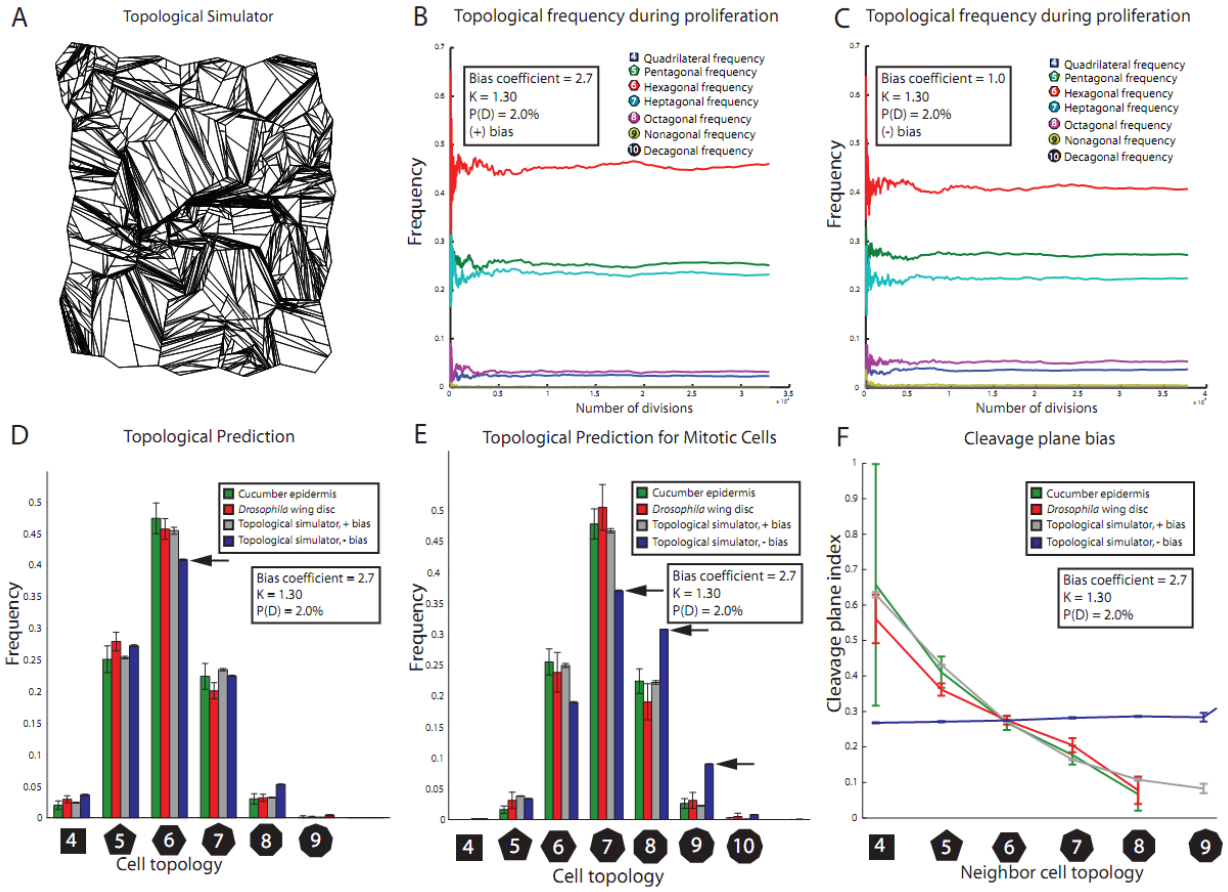
A
Topological Simulator
B
Topological frequency during proliferation
Bias coefficient = 2.7
K = 1.30
P(D) = 2.0%
(+) bias
Quadrilateral frequency
Pentagonal frequency
Hexagonal frequency
Heptagonal frequency
Octagonal frequency
Nonagonal frequency
Decagonal frequency
Frequency
Number of divisions
C
Topological frequency during proliferation
Bias coefficient = 1.0
K = 1.30
P(D) = 2.0%
(-) bias
Frequency
Number of divisions
D
Topological Prediction
Cucumber epidermis
Drosophila wing disc
Topological simulator, + bias
Topological simulator, - bias
Bias coefficient = 2.7
K = 1.30
P(D) = 2.0%
Frequency
Cell topology
E
Topological Prediction for Mitotic Cells
Cell topology
F
Cleavage plane bias
Cleavage plane index
Neighbor cell topology

Figure S6:

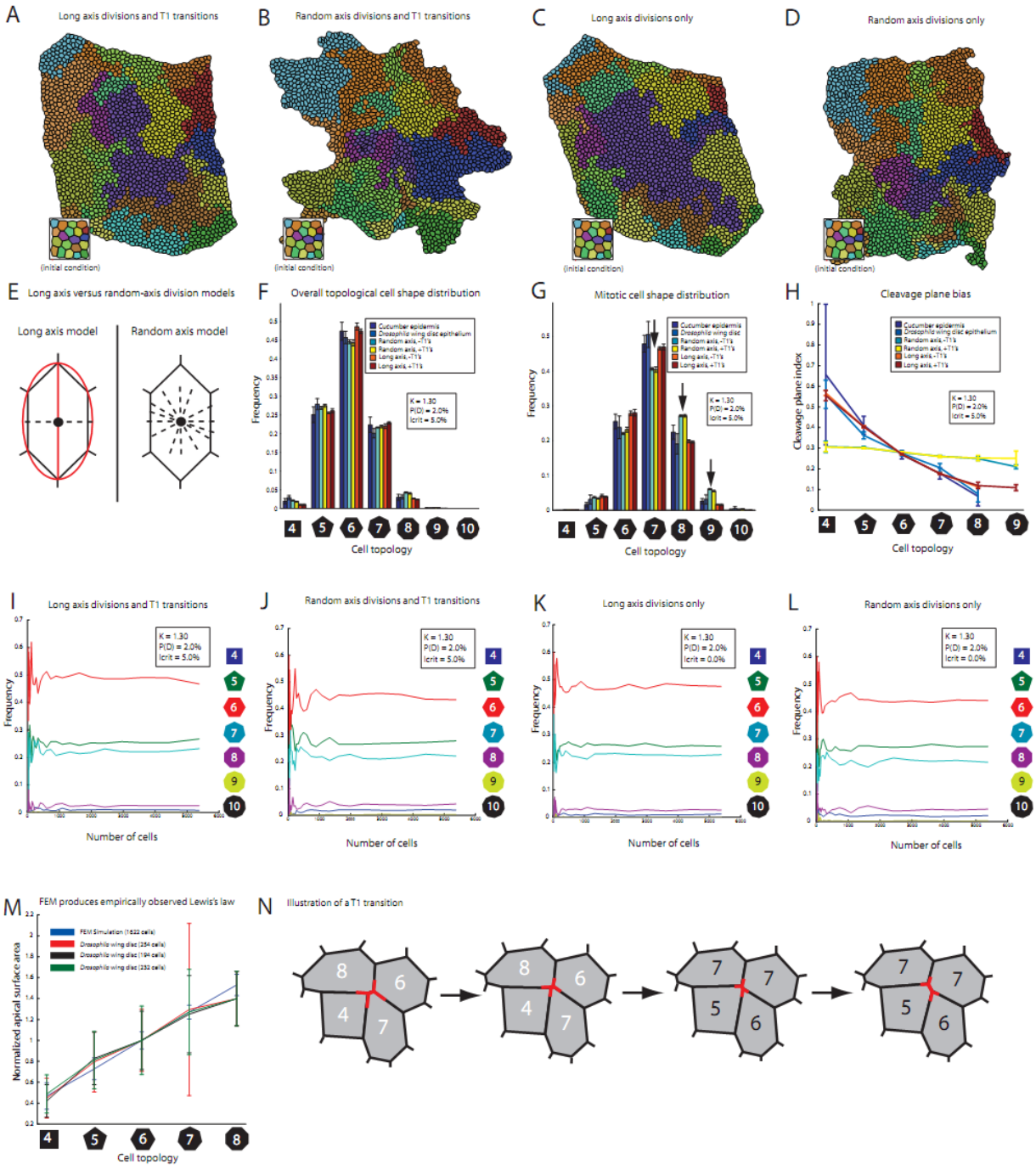
A
Long axis divisions and T1 transitions
B
Random axis divisions and T1 transitions
C
Long axis divisions only
D
Random axis divisions only
(initial condition)
E
Long axis versus random-axis division models
Long axis model
Random axis model
F
Overall topological cell shape distribution
G
Mitotic cell shape distribution
H
Cleavage plane bias
Frequency
Cleavage plane index
Cell topology
I
Long axis divisions and T1 transitions
J
Random axis divisions and T1 transitions
K
Long axis divisions only
L
Random axis divisions only
Number of cells
M
FEM produces empirically observed Lewis's law
Normalized apical surface area
N
Illustration of a T1 transition

II. Figure legends for supplemental Figures S1-S6 and supplemental Movie S1:

Figure S1, related to Figure 1: A diagram for the mechanical relaxation algorithm.

(A) Diagram for an individual cell as represented by the relaxation algorithm. Red-filled circles represent nodes, which are assumed to behave as point masses during relaxation. Jagged lines represent ideal springs, which provide a contractile force to the cellular edge lengths. Internal pressure, which is assumed to be uniform in all directions, and which opposes this contractile force, is diagrammed using arrows. **(B)** Structural legend. The relaxation algorithm is implemented in terms of a set of interconnected nodes, edges and faces. The notation F(i) refers to the set of faces to which node i belongs. Except for cases along the boundary, in our simulations each node will belong to exactly three faces. Similarly, except in boundary cases, the i^{th} node will have exactly three edges E(i) impinging on it. The notation d_{ij} refers to the distance between nodes "i" and "j." **(C)** The relaxation algorithm is implemented in terms of the sum of three forces acting at the nodes. The first, tension, is implemented in terms of an ideal spring, whose force is proportional to the distance between the spring's current length and its rest length. The second force, internal pressure, is modeled as an ideal gas. The third force, friction, opposes node motion and is implemented in order to bring the system towards a minimal energy configuration. **(D)** The general form of the equations used to numerically solve for the system's equilibrium, in terms of forces and structural relationships between nodes, faces, and edges.

Figure S2, related to Figure 3: Tissue measurements reveal the kinetics and mechanisms operating during cell shape emergence in the *Drosophila* wing disc epithelium.

(A) The conditional mitotic index, P(D|N), of a polygonal cell depends its number of sides, N. For example, about 5% of heptagons (N=7) are dividing, whereas about 10% of octagons (N=8) are dividing. The star for nonagons (N=9) indicates that the sample size is too small to reliably estimate the standard deviation. **(B)** Polygonal cells exhibit a strong preference to divide their junctions evenly. On the horizontal axis, zero indicates perfect division symmetry, which can only be achieved by cells when N is even (solid lines). For smaller N values, a greater frequency of divisions is perfectly symmetric. **(C)** Neighbor cell topology biases cleavage plane orientation in dividing cells (see main text, Figure 3). **(D)** Both in *Drosophila* and in *Cucumis*, the distribution

of mitotic cells recapitulates the global distribution of cell shapes, except that it is shifted by a single polygon class. **(E)** A schematic diagram illustrating two metrics: relative arc length and relative side length. Relative side length is measured in terms of a neighbor cell's perimeter. It is defined as the fraction of that perimeter. Relative arc length of a cell, by contrast, is the fraction of the internal angle in the neighboring cell, as measured from the center of mass to the pair of shared vertices. **(F)** Neither relative side length (*red*) nor relative arc length (*green*) varies substantially as a function of polygon class when the reference cell is non-mitotic (resting). **(G)** Relative side length does not vary substantially as a function of topology when the reference cell (see panel E) is a rounded-up cell, just prior to cytokinesis. **(H)** Based on empirical resting cell geometries, a long-axis division mechanism (*red*) predicts a stronger cleavage plane bias than a randomly-oriented division axis (*green*). **(I)** The distribution of cell shapes surrounding mitotic cells is almost identical to the distribution of cell shapes in the tissue as a whole.

Figure S3, related to Figure 4: A long-axis division mechanism, in combination with cucumber cell geometry, is sufficient to reproduce the inferred cleavage plane bias for *Cucumis sativus.*

(A) Maximum intensity projections of Z-stack, confocal images of cucumber epidermis stained with Calcofluor white. For image clarity, white content has been adjusted using Adobe Photoshop. Ellipses of best fit are shown in red, with dotted lines representing the short axis, or presumed cleavage plane. Red lettering gives the polygon class of neighboring cells in the short axis position. **(B)** Cells in the short axis position have a skewed distribution as compared with cells in the general population for cucumber epidermis. To generate the population of 1002 cells in the short axis position, in an unbiased manner, we selected 501 cells having the (shifted) distribution of cell shapes measured in Lewis's population of dividing cells (Lewis, 1928). Ellipses were then fit to these cells, which determined the population of the 1002 neighbors in the short axis position. Note the enrichment for 4-sided and 5-sided cells in the short-axis cell population. **(C)** The polygon-class specific enrichment factors (as compared with the overall epidermis) closely match between Lewis's 1928 study of 1000 cells on the ends of 500 cleavage planes, and our study of 1002 cells on the ends of 501 short axes. **(D)** The predicted cleavage plane bias correspondingly matches the inferred cleavage plane bias measured from Lewis's original data (Lewis, 1928).

Figure S4, Related to Figure 5: Cleavage plane bias is robust to cell size differences in the N-sided cell, *N*.

(A) For the case of quadrilaterals, the (effective) attraction of the short axis is robust to large variation in cell size. **(B)** Bias due to a hexagonal cell of variable size is an unstable point due to symmetry breaking. Slight perturbation above or below the target apical surface area is sufficient to rotate the long and short axes by 90˚. **(C)** For the case of octagons, the (effective) repulsion of the short axis is robust to cell size differences, except for cases of unnatural and excessive cell enlargement (far right). **(D)** Based on live imaging analysis of 60 local neighborhoods surrounding dividing cells in the *Drosophila* wing disc, neighbor cell size at interphase is not likely to play a role in orienting the division plane. Excluding the area of the central mitotic cell, interphase cell areas were normalized to the total apical area of each local neighborhood (the average normalized area of a cell in each neighborhood is 1.0). Of the 116 observable cells in the cleavage position at cytokinesis, the average normalized area for the same cells at interphase was 1.0016 with a standard deviation of .2202. Hence, cells in the cleavage plane position at cytokinesis are of approximately average size at interphase.

Figure S5, related to Figure 6 (upper panels): A topological simulator based on empirically measured division kinetics accurately captures the steady-state dynamics of the tissue, but only when cleavage-plane bias is present.

(A) The topological simulator does not model cellular mechanics, but does explicitly keep track of topological neighbor relationships. Division likelihood, symmetry, and bias are matched to empirically measured statistics (see Figure S2A-C). **(B-C)** In the presence or in the absence of bias, the system has approximately reached steady-state after 30000+ divisions, after starting from an initial condition of 60% hexagons, 20% pentagons, and 20% heptagons. **(D-F)** "K" refers to the exponential constant specifying the probability of cell division (see Figure S2A). P(D) is the mitotic index, or proportion of all cells that are dividing per time step. The "bias coefficient" governs the strength of the cleavage plane bias (see Extended Experimental Procedures, section 6). **(D)** At steady-state, in the absence of cleavage plane bias, the frequency of hexagons is about 4% lower (*black arrow; blue*) than when cleavage plane bias is present (*gray*). **(E)** Without bias, the distribution of dividing cells shows pronounced alterations. Note the large differences in heptagonal, octagonal, and nonagonal frequencies in the presence versus absence of bias (*black arrows*, *gray versus blue*). Note also the comparison with the empirically measured distributions in *Drosophila* (*red*) and *Cucumis (green)*. **(F)** The

topological Monte-Carlo framework closely captures the empirically observed cleavage plane bias.

Figure S6, related to Figure 6 (lower panels): A finite element simulator based on empirically measured parameters accurately captures the steady-state dynamics of the tissue, but only when long-axis divisions are used.

(A-D) Graphical output from the finite element model. T1 transitions result in more regular tissue patterns, and allow the cells to rearrange in order to relieve stress. Note that panels (A-D) use toroidal (wrapping) boundary conditions. Therefore, the shapes of the tissue boundaries should not be taken to indicate tissue regularity. **(E)** A graphical comparison between long-axis divisions and (uniform) random-axis divisions. **(F)** Long-axis divisions result in an increased hexagonal frequency relative to random-axis divisions. T1 transitions do not qualitatively alter this result. The FEM closely captures the empirically observed p* distribution using the *in vivo* parameters. **(G)** The shape of the mitotic cell distribution is substantially altered relative to the empirical values when random-axis divisions are used instead of long-axis divisions (*black arrows*). This suggests that cleavage plane bias plays a role in setting the topological division rates (and hence the mitotic shift, see figure S2D), and in the kinetics of side gaining. **(H)** Using random-axis divisions effectively removes the cleavage plane bias. By contrast, long axis divisions faithfully reproduce the empirically observed cleavage plane biases in fly and cucumber. **(I-L)** The system is approximately stable after 5300 divisions. **(M)** Based on polygon-specific volume constraints, the FEM simulation approximately obeys Lewis's linear law of areas, as judged by a comparison with empirical data. **(N)** During a T1-type transition, a pair of tri-cellular junctions moves closer together as the edge separating them shrinks. In our simulations, the T1 transition is only implemented if the edge length separating these two vertices drops below a critical fraction, l_{crit} of the average edge length throughout the sheet. Just prior to the transition, the edge length has shrunk to zero, forming an unstable 4-way junction (not shown). Following this unstable intermediate, the system relaxes with the opposite orientation, resulting in the generation of a new edge. Note that one pair of cells gains one edge each, whereas the other pair of cells loses one edge each.

Movie S1, related to Figure 4: A third instar wing imaginal disc proliferating in *ex vivo* culture. The septate junctions are marked with nrg-GFP; chromatin is marked with H2RFP. Chromosome movement is clearly visible at anaphase. Note the dynamic nature of cell shape as cells progress from interphase, through mitotic rounding, and into cytokinesis. The movie covers a 2-hour period.

III. Extended Experimental Procedures:

(1) Algorithm for computing the minimal energy configuration of local cellular neighborhoods

To understand how the shape of a cell is influenced by the shapes of its surrounding neighbors, we implemented an algorithm to find minimal energy configurations of cell packing, similar to that described by Prusinkiewicz and Lindenmayer (1990). Here, we discuss the algorithm's functional form, boundary conditions, parameters, and implementation. For a diagram of the algorithmic details, see Figure S1.

The algorithm assumes that, at equilibrium, apical cell areas are determined by a balance between internal cellular pressure and contractile forces along cellular edge lengths (Figure S1A). For relaxation, cells are modeled as two dimensional polygons at their apical surface, and referred to as "faces." Nodes and edges are modeled, respectively, as point masses and ideal springs (Figure S1A). The assumption that the nodes have mass is irrelevant at equilibrium. Internal pressure is modeled as an ideal gas. During relaxation, damping is achieved using friction, proportional to node velocity. These relationships are captured as a system of coupled ordinary differential equations:

$$q_i \frac{d^2}{dt^2}\left(\vec{x_i}\right) = \left[\sum_{\substack{j\in E(i)\\ k\in F(i)}} \vec{T_{ij}} + \frac{1}{2}\vec{P_{ij}}(k)\right] - C_i \frac{d}{dt}\left(\vec{x_i}\right) \qquad (1)$$

where "q_i" is the mass of the i^{th} node, $\mathbf{x_i}$ is the 2D vector position of node i, d/dt and d^2/dt^2 are time derivative operators, E(i) refers to the set of edges incident to node i, F(i) is the set of faces to which node i belongs, $\mathbf{T_{ij}}$ refers to the tensional force exerted on

node i by the spring connecting nodes i and j, C_i is the friction coefficient for node i, and $\mathbf{P_{ij}(k)}$ is the force exerted on nodes i and j due to internal pressure from face k (to which nodes i and j belong). The magnitude for the force due to internal pressure is given by the following expression:

$$\left\| P_{ij}(k) \right\| = \frac{d_{ij} n_k H_k}{A_k} \tag{2}$$

where n_k is the number of moles of ideal gas inside face k, A_K is the area of face k, d_{ij} is the distance between nodes i and j, and H_k encapsulates the universal gas constant as well as the temperature. We assume without loss of generality that the height of all polygonal cells is 1. Hence, to recover the force exerted by the ideal gas, we simply multiply the pressure expression by d_{ij}, which is equivalent to the area of the interface between the two cells.

The magnitude of the tension is captured by the following Hookean relation:

$$\left\| T_{ij} \right\| = G_{ij}(d_{ij} - l_0) \tag{3}$$

where G_{ij} is the stiffness constant for the spring placed between nodes i and j, and l_0 is the rest length.

For our simulations, parameters were chosen to be equal for all cells. The following values were used: $q_i = 0.0001$, for point masses; $l_0 = .0001$, for the rest lengths of springs; $C_i = 2.0$, for the friction coefficients; 1.0, for the product $n_k H_k$; and $G_{ij} = 5.0$, for spring stiffness constants. Rest lengths were chosen such that cellular edge lengths

were much longer than the rest lengths of springs at steady-state, thus placing them under considerable tension. Friction coefficients were chosen such that the system would approach steady-state within a reasonable time frame. We used free boundary conditions, where the central cell and its immediate neighbors are surrounded by three outer rows of hexagonal cells to mitigate edge effects. Equations were integrated numerically using the ode45 solver in MATLAB (Mathworks). Integration was continuted until the total squared velocity of the nodes summed over the entire cell sheet dropped below an arbitrary threshold cutoff, taken to be 0.003.

(2) Description of simulated cell divisions:

In the main text, we use two different models of cell division: random-axis divisions and long-axis divisions (Figure S6E). Here, we specify the algorithms and implementation methods that were used for each. The same algorithms were used for both simulated cell shapes and experimental cell shapes.

(2.1) Computation of the cellular long and short axes: We defined the long and short axes of a cell in terms of an elliptical fit to the cell's vertices. To determine the ellipse of best fit, we used a direct least-squares fitting procedure, which has been described elsewhere (Fitzgibbon et al., 1999). For an improved framework that is more numerically stable, please see the following URL: <http://research.microsoft.com/en-us/um/people/awf/ellipse/fitellipse.html>.

(2.2) Definition of the long-axis division: The division plane for a long-axis division is taken to be the short axis of the ellipse of best fit, which bisects the

long axis. There is one additional caveat, which is that we require the division plane to pass through the cell's centroid. This is achieved by fitting a line through the centroid with the same orientation as the short axis. For polygonal cells, the distance between the centroid and the center of the ellipse is very small.

(2.3) Definition of the randomly oriented division: The random-axis division model describes the division plane as a straight line passing through the cell's centroid, with an orientation drawn from a uniform random distribution, from 0 to 2π.

(2.4) Determination of which neighbor cells are in the division plane position: The neighbor cells in the division plane position are determined by finding the intersection points of the line representing the division plane with the polygonal cell cortex. The polygonal neighbors sharing the intersected edges are considered to be in the division plane position.

(2.5) Computation of the cellular centroid: The centroid (C_x,C_y) is computed in terms of the N vertices, where the set of coordinates for vertex i is denoted (x_i,y_i). The vertices are assumed to be ordered with counter-clockwise orientation, where vertex i=0 is equivalent to vertex i=N. The centroid is found in the following manner (Bashein and Detmer, 1994):

$$C_x = \frac{1}{6A}\sum_{i=0}^{N-1}(x_i + x_{i+1})(x_i y_{i+1} - x_{i+1} y_i)$$
$$C_y = \frac{1}{6A}\sum_{i=0}^{N-1}(y_i + y_{i+1})(x_i y_{i+1} - x_{i+1} y_i) \quad (4)$$

The area *A* of the polygon is found as:

$$A = \tfrac{1}{2}\sum_{i=0}^{N-1}(x_i y_{i+1} - x_{i+1} y_i)\,. \qquad (5)$$

(3) Empirical analysis of proliferation parameters in the *Drosophila* wing disc:

In order to understand the role of cleavage plane bias *in vivo*, it was necessary to understand the dynamic context in which the bias operates. To this end, we empirically measured the parameters governing cell shape emergence in the *Drosophila* wing disc. Below we describe how the empirical rate constants for the *Drosophila* wing disc were either directly computed or statistically inferred from our measurements of cytokinetic figures (Figure 3E; Experimental Procedures). For all probabilities and rate parameters described below, the relevant time scale, τ, for the measurement is the duration of M-phase.

(3.1) Polygon-specific cleavage plane bias: From a sample of 420 dividing cells and their 2946 immediate neighbors, cleavage plane bias was computed as the fraction of N-sided cells in the division plane furrow (Figure 3; Experimental Procedures).

(3.2) Polygon-specific division equality measurements: For all mitotic polygon classes, we have measured the fraction of M-sided cells that give rise to a J-sided daughter, where M and J are arbitrary. We can summarize these measurements as a matrix, which is referred to as the division kernel. The division kernel was inferred from 418 cytokinetic figures (Figure 3E; Experimental Procedures). Kernel values were computed according to the formula

$M+4=N_1+N_2$, where M is the topology of the mother cell, and N_1 and N_2 are the topologies of the two daughter cells.

(3.3) Mitotic index for the *Drosophila* wing disc: The mitotic index over all polygon classes, P(D), is defined to be the percentage of cells that are in M-phase. Experimentally, P(D) is calculated as an average percentage of cells in fixed tissues that positively stain for M-phase markers. We have measured P(D) for the *Drosophila* wing disc in 96-hour wandering larvae to be approximately 1.76% (+/- . 17%, corrected 95% confidence interval).

(3.4) Polygon-specific mitotic indices for the *Drosophila* wing disc: We have found that in the *Drosophila* wing disc, the fraction of cells dividing in any one polygon class may differ from the overall mitotic index P(D), which is an average over the different polygon classes. Therefore, there is a *conditional mitotic index*, P(D|N), for each polygon class, which gives the fraction of N-sided cells dividing, where N ranges from 4 to 9. Equivalently, P(D|N) can be thought of as the probability in unit time τ that a randomly selected cell is in M phase given that it has N sides. To infer P(D|N), we used Bayes' rule:

$$P(D \mid N) = \frac{P(N \mid D)P(D)}{P(N)} \qquad (6).$$

Here, P(N|D) is the polygonal cell shape distribution for cells that are in M phase, P(D) is the mitotic index, and P(N) is the global distribution of polygon types. P(N|D) has been measured experimentally from 418 cytokinetic figures (Figure 3E; Figure S3D; Experimental Procedures). P(N) was measured in a previous study (Gibson et al., 2006). Based on the assumption that empirical wing disc

epithelial topology has reached steady-state, we infer that the form of P(D|N) is closely approximated (R^2 coefficient >.99) by an exponential function in the number of edges N, with exponential constant, K. This is consistent with previous measurements in plants (Dubertret et al., 1998). To compute K, we used the cftool function in MATLAB (Mathworks). Using all data points (N=4…9), we obtain a K value of approximately 1.25. To visualize the polygon-specific mitotic index for each polygon class, see Figure S2A.

(3.5) Rates of T1 transitions in the *Drosophila* wing disc: Based on live imaging studies and the contiguity of marked cell clones, cellular rearrangement is rare in the *Drosophila* wing disc. Based on analysis of 2-cell clones, it can be inferred from a previous study that about 6% of edges undergo T1 transitions per 11 hours (Gibson et al., 2006). For an illustration of a T1 transition, see Figure S6N. The 6% figure may be an over-estimate, because it is based primarily on dividing cells, which are subjected to increased mechanical stress during mitosis. If T1 transitions are more common under mechanical stress, then the true rate of cellular rearrangement might be lower than 6%.

(3.6) Lewis's law of linear areas in *Drosophila*: In the context of a monolayer cell sheet, the average surface area of an N-sided polygonal cell is approximately linear in the value of N, a relationship known as Lewis's law (Farhadifar et al., 2007; Lewis, 1928; Patel et al., 2009; Rivier and Lissowski, 1982). Here we have quantified this relationship for the *Drosophila* wing disc. From three digitally annotated cell sheets (see Experimental Procedures), we normalized the cell

areas of each sheet with respect to the average hexagonal cell area, and then grouped the cells by polygon class. For the data set, we discarded all 9-sided cells, which were rare, and also one octagonal outlier cell. For each sheet, we then used the cftool in Matlab (Mathworks) to fit a straight line to the average normalized cell area, as a function of polygon class. The slopes found, were, respectively, .2404, .3068, and .3357, for an average of .2943 (with standard deviation of .0489). By comparison, the slope for FT Lewis's cucumber cells (when normalized to the average hexagonal area, and excluding nonagons) is closer to .2247 for non-dividing cells, and .104 for dividing cells (Lewis, 1928).

4. Analysis of geometric parameters in the *Drosophila* wing disc

In order to test whether side length might play a role in cleavage plane bias, we annotated and analyzed the apical geometry of epithelial cells in the *Drosophila* wing disc. Our measurements (figure S2F-H) suggest that this is unlikely.

(4.1) Annotation of local neighborhoods of resting cells: Local neighborhoods surrounding 205 resting, non-mitotic cells were annotated by hand using Microsoft Powerpoint. Multiple focal planes were used to ensure accuracy of annotations. We used custom-built software to digitize the annotations for analysis in MATLAB.

(4.2) Analysis of local neighborhoods: Two metrics were used to assess topological variability of neighbor side length in resting cells (figure S2E). The first metric is linear side length, measured from the first shared node to the

second of the shared edge. We normalized this length to the total linearized perimeter of the central cell (i.e. the cell whose neighbors are being studied). The second metric is normalized arc length, which is simply the angle between the two shared nodes, as measured from the central cell's center of mass, normalized by 360° (Figure S2E). We found that neither metric showed substantial difference as a function of polygon class (Figure S2F).

(4.3) Measurements of rounded cell side lengths: Side lengths of 100 rounded, mitotic cells were measured by hand, taking curvature into account, using ImageJ. Cell side lengths were normalized to the total perimeter of each rounded cell. We did not observe significant variability of the average normalized side length as a function of polygon class (Figure S2G).

(4.4) Cleavage plane bias as predicted by resting cell geometry: In order to estimate the cleavage plane bias that would be expected from resting (non-mitotic) cell geometry in *Drosophila*, we computed an approximate cleavage plane bias based on a long-axis model of cell division. For comparison, we considered a uniform-random cleavage plane orientation, which was drawn from a random-number generator in MATLAB (Mathworks). We found a significantly stronger bias using the long-axis division rule (Figure S2H).

5. Time lapse analysis of cell division in the *Drosophila* wing imaginal disc:

In order to test whether cells in the *Drosophila* wing imaginal disc actually obey a long-axis division mechanism, we used time-lapse microscopy to study wing disc epithelial cells as they progressed from interphase through cytokinesis in *ex vivo* culture. Time lapse movies were recorded for the entire wing blade region at 63X magnification. The focal plane was adjusted manually, and guided by the neuroglian-GFP marker to stay at the level of the septate junctions. For an example, see Supplemental Movie S1.

(5.1) Dataset description: A total of 210 cells undergoing the division process were annotated, of which 198 started in interphase, as judged by cellular morphology. The geometry of each cell was recorded using the ImageJ polygon selections tool, with nodes placed liberally in order to accurately record cellular morphology. For each such annotation, the orientation for the ellipse of best fit (computed using the ImageJ measuring tool) was recorded. Upon cytokinesis, the cell morphology was again annotated, and a second ellipse fit was made. The recorded deviation of division from the interphase long axis (see Figure 4B) was taken to be the angle between the two measurements. Every scoreable dividing cell was measured on the epithelium, with the exception of cells on compartment boundaries, or those rare cells that entered mitosis at the same time as an immediate neighbor. The latter were not scored to control for

hypothetical mechanical influences on the spindle due to the neighboring cell's expansion.

(5.2) The correlation between the orientation of cytokinesis and orientation of the interphase long axis is roughly independent of time: Based on analysis of 198 dividing cells, we found that the time lag between the measurement of the interphase long axis, and the final measurement of the orientation of cytokinesis, made very little difference in the correlation between the two variables (data not shown). Based on a linear interpolation to the data, on average, the deviation increased by less than one degree for each hour that elapsed between the two measurements. For instance, for those cells dividing about 20 minutes after the initial interphase measurement, the eventual cytokinetic orientation was predicted to be about 26 degrees off the long axis on average. For cells undergoing cytokinesis approximately 220 minutes after the initial measurement, the deviation is about 29 degrees. Therefore, the orientation of a cell's long axis appears to remain relatively constant with time.

(5.3) The average deviation from a long-axis division mechanism decreases as a function of relative length of the long axis to the short axis: Based on analysis of 198 dividing cells, we found that the deviation from the long-axis division mechanism was partly a function of cell geometry. Specifically, the larger the ratio of the long axis length to the short axis length, the smaller the deviation from a long-axis division mechanism (data not shown). Specifically,

cells having a long- to short-axis length ratio close to one showed a deviation from the long axis division mechanism close to the theoretically predicted value of 45° for a random cleavage plane. By contrast, cells having a well-defined long axis more closely obeyed the long-axis division rule. A linear fit to the data suggests that a cell having a long- to short-axis length ratio at or above approximately 4.5 should perfectly obey the long-axis division mechanism (data not shown). To conclude, this suggests that in the *Drosophila* wing disc, the spindle orientation mechanism is sensitive to the degree of elongation of the cell.

(5.4) Incorporation of the measured deviation into the original cleavage plane bias prediction: The average measured deviation between the interphase long axis and the eventual cytokinetic orientation was approximately 27 degrees. To test the influence of this deviation on cleavage plane bias, we re-computed the bias using a 27-degree deviation from the short axis to predict the cleavage plane. We controlled for the influence of topological relationships by using the same local neighborhoods as were measured from the empirical data (see Figure 3). Interestingly, when including the measured deviation, we obtained a much improved bias prediction which is significantly closer to the empirically measured values (see Figure 4C; compare red and black curves). A similar result is obtained when the deviation from long-axis division is simulated as Gaussian noise with a 27 degree standard deviation (data not shown).

(5.5) Cell size is not predicted to play a strong role in guiding the mitotic cleavage plane: We followed the immediate neighbors of 60 dividing cells as those cells progressed from interphase, through prophase, and into cytokinesis. To test the hypothesis that cell size might be capable of biasing cleavage plane orientation, we studied the interphase sizes of those neighbor cells which later on occupied the cleavage plane position of their mitotic neighbor. Out of 120 possible such neighbors in the cleavage plane (two for each of the 60 dividing cells), we were able to observe 116. We normalized the areas of such cells based on the average neighbor area value for each local neighborhood. Based on the data (see Figure S4D), neighbor cell size is not likely to play a strong role in orienting the cleavage plane. The distribution of neighbor cell sizes in the cleavage plane position is, on average, very close to the average size for a cell neighboring a dividing cell (ie, close to 1 on average). For the 116 cells in the cleavage plane position, we computed a value of 1.0016 for the average normalized area, and a standard deviation of .2202.

6. Empirical analysis of proliferation parameters in the dataset for *Cucumis*:

Polygon-specific cleavage plane bias in Cucumis: To compute the cleavage plane bias for the cucumber, we used an historical data set gathered by F. T. Lewis (1928) which includes three cell shape distributions of interest for cucumber cells. The first is the tissue-wide distribution of polygonal cell shapes (Lewis, 1928), P(N), which closely resembles the distribution of cell shapes in a variety of other organisms (Gibson and Gibson, 2009), including *Drosophila* (Figure S2D, *compare red and green distributions for all cells*). The second distribution measured by Lewis is that of mitotic cells, P(N|D), which again closely resembles the distribution seen in *Drosophila* (Figure S2D, *compare red and green distributions for mitotic cells*). The third distribution is P(N|G,B). This is essentially the distribution of polygonal cell shapes located in the division plane position of cytokinetic cells (Lewis, 1928).

It is instructive to consider the ratio of the number of N-sided cells in the division plane position (i.e. the cells having edges bisected by mitotic cleavage planes) to the number of N-sided cells throughout the tissue. Upon computing this ratio, it is apparent that there is strong enrichment for some polygon classes over others in the division plane position. Below, using only the very mild assumption that cell divisions are sparsely distributed throughout the tissue, we formalize this reasoning and compute a very close approximation to the cleavage plane bias for the cucumber.

The cleavage plane bias is formally represented as P(G|N,B), which can be understood as the *fraction of N-sided cells* neighboring a mitotic cell that are in the

division plane position. In order to compute this from existing data, we can use Bayes' rule. For the cucumber, we have expressed P(G|N,B) in terms of 5 other distributions:

1. **P(N|G,B)**: This is the distribution of cell shapes located in the division plane position of cytokinetic cells, as measured by FT Lewis (1928).
2. **P(B|G)**: This is the fraction of cells occupying the division plane position of mitotic cells that gain a side, which is true for all such cells. Therefore, P(B|G) is always equal to one.
3. **P(G)**: This is the fraction of all cells in the division plane positions of mitotic cells. Assuming sparse divisions, this is equal to twice the mitotic index, or 2 times P(D).
4. **P(N|B)**: This is the distribution of cell shapes for cells that border a cytokinetic cell. Both based on our studies of this distribution in *Drosophila* (see Figure S2I) and based on maximum entropy estimates (Peshkin et al., 1991), this distribution is closely approximated by the tissue-wide distribution of cell types, P(N).
5. **P(B)**: This is the fraction of cells neighboring mitotic cells. Assuming sparse divisions, and based on the distribution of dividing cells (Figure S2D), which have an average of 7 neighbors, this is approximately equal to 7 times P(D).

Using Bayes' rule, we can approximately compute the cleavage plane bias in the following manner:

$$P(G \mid N, B) = \frac{P(N \mid G, B)P(B \mid G)P(G)}{P(N \mid B)P(B)} \quad (7).$$

As discussed above, P(B|G) is equal to one, and the ratio of P(G) to P(B) is almost exactly 2/7, because these two quantities are, respectively, 2 and 7 times the mitotic index, P(D). Moreover, P(N|B) is very well approximated (see Figure S2I) by P(N). Therefore, we find that the cleavage plane bias for cucumber epidermis is well approximated by the following:

$$P(G \mid N, B) \approx \frac{2P(N \mid G, B)}{7P(N)} \tag{8}$$

Both P(N|G,B) and P(N) were measured by F. T. Lewis using sample sizes of 1000 cells each, which enables us to estimate the error on the calculation. Remarkably, the cleavage plane bias for cucumber is almost indistinguishable from that of *Drosophila* (see Figure 3H).

7. Empirical analysis of cell geometry in *Cucumis* epidermis.

To test whether a naïve long-axis model for cell division is sufficient to generate cleavage plane bias in *Cucumis*, we analyzed the epidermis of freshly-collected *Cucumis* specimens using confocal microscopy. For sample preparation details, see Experimental Procedures. The specimens, being approximately 10cm in length, and 2cm in diameter, were similar in size to those used in Lewis's original study (Lewis, 1928). The steps in our analysis are outlined below.

(7.1) The epidermis-wide distribution of cellular shapes: We first gathered empirical statistics for the epidermis-wide distribution of polygonal cell shapes. Cells were scored in terms of the number of neighbors, from large, contiguous

epidermal regions of 400 cells or more. In total, we scored 2464 cells, which have the distribution shown in Figure S3B (*green*).

(7.2) Unbiased selection of a shifted cell shape distribution: We next selected cells having the same polygon class distribution as the dividing cells collected in Lewis's original study, which is shifted to have a heptagonal mean (Lewis, 1928). For each class of N-sided cell, we selected contiguous regions of tissue, and densely scored the N-sided cells in the region before enlarging the territory to look for additional cells. We therefore obtained an unbiased sampling of cells, selected solely on the basis of polygon class, having the same distribution of polygonal shapes as the mitotic cells studied by Lewis.

(7.3) Annotation of the selected cell shapes, and determination of neighbors in the short-axis position: For each of the selected 501 cells, we manually annotated the polygonal cell geometry using the Polygon Selections tool in ImageJ. Based on these annotations, we used the measure tool in ImageJ to compute the ellipse of best fit, and a custom-made macro to plot the ellipse, along with the long and short axes. The short axis impinged on exactly two neighboring cells for each ellipse, and these were taken to be the neighbors in the cleavage plane position. From the sample of 501 annotated cells, we obtained 1002 cells in the cleavage plane position, which have the distribution shown in Figure S3B (*red*).

(7.4) Computation of topological enrichment: Note than in Figure S3B, relative to the epidermis-wide distribution of cellular shapes (*green*), the frequencies of four-sided and five-sided cells are higher in the short-axis position (*red*), whereas the frequencies of heptagons and octagons are lower. To quantify the enrichment or under-representation of each polygon class, we plotted the ratio of the short-axis measurements to the epidermis-wide measurements (Figure S3C, *blue*). For comparison, we also plotted the enrichment pattern for the cleavage plane position from Lewis's original data (Figure S3C, *black*). Note that in both cases, there is a very clear and similar trend. Four-sided cells are enriched approximately two-fold, hexagons show approximately no enrichment, and octagons are under-represented.

(7.5) Prediction of cleavage plane bias: Given the similar enrichment patterns in the short axis position of our randomly selected sample, and the cleavage plane position of the mitotic cells in Lewis's original dataset, we decided to compute the predicted bias as based on the short-axis position data using the same procedure used in Extended Experimental Procedures, section 6. This computation tests whether a short-axis division mechanism, combined with the epidermal geometry of *Cucumis*, is sufficient to predict the cleavage plane bias. Notably, when plotted against the cleavage plane bias inferred from Lewis's original data, the two curves are in close agreement (Figure S3D). We conclude that a naïve short-axis division mechanism is sufficient to generate cleavage plane bias in *Cucumis*.

8. Description of global models of tissue proliferation:

To understand the interaction between cleavage plane bias and cell shape on a tissue-wide scale, we simulated the dynamics of cell shape emergence in the context of proliferative epithelial simulations using the empirically measured parameters (see Extended Experimental Procedures, section 3). Here, we describe the details for how these simulations were implemented.

(8.1) *Topological Monte-Carlo simulations of tissue proliferation:*

In order to study the effects of cleavage plane bias in an abstract, topological framework independent of geometric parameters, we used a topological Monte-Carlo simulator of epithelial proliferation based on the empirically measured topological division kinetics (Figure S2A-C; see Extended Experimental Procedures, section 3). A non-empirical version was analyzed in a previous theoretical study (Patel et al., 2009). This framework permits simulation of very large cell sheets (on the order of 30,000 cells or more) that would not be practical in a more geometrically realistic, finite element simulation (Extended Experimental Procedures, section 8.3).

The timing model for the topological simulator is based on the exponential form for the polygon class-specific division probabilities. Cells are chosen for division, with replacement, with probability proportional to e^{KN}, where K is a constant set to 1.3 (Extended Experimental Procedures, section 3.4), and N is the polygon class. The time

step is defined in terms of the mitotic index, making it approximately equal to the duration of M-phase in the cell cycle. Consistent with empirical measurements, we have chosen a mitotic index of 2% for each time step. To avoid ambiguous cases in which neighbor cells might influence each others' division probabilities in the same time step, we have forbidden cells that are immediate neighbors from dividing. This is achieved using a rejection procedure that simply re-draws the entire sample of dividing cells if the previous random draw selected at least one pair of immediate neighbor cells.

Once a cell has been chosen to divide, the next step is to specify its division plane. Topologically, this is equivalent to deciding which of the dividing cell's edges will be bisected by the division plane, which is modeled as a straight line. The first edge to be bisected is selected stochastically. This is accomplished by assigning each of the dividing cell's edges a weight according to the topology of the neighbor cell sharing that edge (recall that every edge is shared by exactly two cells). A single edge is selected from the dividing cell's total complement of edges with probability proportional to its weight. Hence, the topological weights determine the likelihood that a neighbor with a given topology will occupy the cleavage plane position. To assign weights, the function used is an inverse exponential, with a base equal to 2.7, which was determined by trial-and-error. To illustrate, a pentagon is 2.7 times as likely as a hexagon to occupy the cleavage plane position, and so on. Intuitively, cleavage plane bias can be removed in this framework by specifying a base of 1.0, in which case all topological neighbors are

equally likely to occupy a division plane position. Once the location of the first edge has been determined, a new tri-cellular junction is formed in the center of the chosen edge. The second edge is specified by stochastically sampling from the empirically measured division kernel (see section 3.2 of the Extended Experimental Procedures; Figure S2B), which specifies how evenly the cells divide up their junctions. In most cases, these two constraints are sufficient to specify the division plane. Occasionally, two possible division orientations are equally likely, in which case the weighting scheme is used a second time with identical topological weights to decide (stochastically) between the two choices. Once the second edge is specified, a tri-cellular junction is inserted into the chosen cellular edge, and the two new tri-cellular junctions are then connected to result in a pair of daughter cells.

(8.2) ***Topological simulation results:***

The topological simulator produces five main results. First, it closely reproduces the shape of the empirically observed cell shape distribution (Figure S5D). Second, it captures cleavage plane bias accurately (Figure S5F). Third, it predicts that hexagonal frequency should drop by approximately 4% in the absence of cleavage plane bias, indicating that cleavage plane bias increases the regularity of the tissue (Figure S5D). Fourth, it captures the distribution of dividing cells accurately when cleavage plane bias is present (Figure S5E). Fifth, when the cleavage plane bias is absent, it predicts pronounced alterations in the distribution of dividing cells. Specifically, it predicts that the frequency of heptagonal cells should decrease, and the frequency of octagons and

nonagons should increase, relative to the empirical case, in the dividing cell distribution (Figure S5E; *black arrows*). Taken together, the above results suggest that cleavage plane bias is an integral part of the maintence of tissue regularity during epithelial sheet proliferation.

(8.3) ***FEM model of tissue proliferation:***

In contrast to the topological simulator, which captures proliferation dynamics and cleavage plane bias in a purely topological framework, the Finite Element Model (FEM) of tissue proliferation incorporates cellular mechanics and geometry to more realistically simulate epithelial sheet proliferation. The mechanical aspects of the FEM have been described elsewhere (Brodland and Veldhuis, 2002; Chen and Brodland, 2000). Briefly, the FEM models apical contractility, cell-cell adhesion, and all other forces along the cellular edge lengths in terms of an equivalent net interfacial tension, γ. Each cellular edge is modeled as a rod-like, constant-force finite element, which generates γ. Cells, which are subject to a volume constraint, are sub-divided into sectors, each having viscosity μ and a Poisson's ratio of zero. Thus, cytoplasm can move within the cell, but not between cells. At each dimensionless time step, subject to the volume constraint, we solved for the resultant network geometry due to interfacial tensions along the cellular edge lengths. We have incorporated polygon-specific volume constraints, V_N, in order to impose Lewis's linear law of polygonal areas (section 3.6 of the Extended Experimental Procedures), using a slope of 0.3 when cell areas are normalized to the

hexagonal mean. In terms of absolute areas, the hexagonal mean was set to 60000. For our simulations, tension γ and viscosity μ were, respectively, 9900 and 20. The initial topological mesh consisted of 20 cells, with a symmetric distribution of 20% pentagons, 60% hexagons, and 20% heptagons. The simulations were run for approximately 5300 divisions. Each data point is averaged over three runs.

The timing model used for the FEM simulator is identical to the one used for the topological Monte-Carlo simulator (section 6.1 of the Extended Experimental Procedures). Once a cell is chosen to divide, its division plane is determined in one of two ways for the FEM. The first option is a uniform random division, which is implemented as a straight line passing through the cell's center, with its orientation drawn from a uniform random distribution, from 0 to 2π. The second option is division of the long axis, which for the FEM is taken to be the principle axis of inertia. This division rule produces cleavage plane bias that is extremely close the empirically measured values (Figure S6H). Here, the division plane is taken to be a straight line through the cell's center, orthogonal to the long axis. We also tested a similar algorithm using the centroid, which yielded similar results (data not shown). Following determination of the division plane, tri-cellular junctions are placed at the two points of intersection of the division plane with neighboring cells' edges, thus forming a pair of polygonal daughter cells.

In addition to mitosis, the FEM framework permits T1-type cellular rearrangements. T1 transitions (Figure S6N) occur when edge lengths shorten beyond a threshold fraction, l_{crit}, of the tissue-wide average edge length. Here, l_{crit} is set to 1/20. A 4-way junction is temporarily formed, created by shrinking the original edge to zero length. Next, the 4-way junction resolves into a new pair of tri-cellular junctions, with the opposite orientation of the previous edge (Figure S6N). The length of the newly-formed edge due to the subsequent T1 transition is specified by the parameter l_{flip}, which is here set to 3 times l_{crit}.

(8.4) ***FEM results:***

The results of the FEM simulator strongly support the predictions of the topological Monte Carlo simulator. For comparison, we can draw a parallel between the long-axis division mechanism used in the the FEM simulator and the topologically biased division plane orientations of the topological Monte-Carlo simulator; both mechanisms re-produce the empirically measured cleavage plane bias (Figures S6H and S5F). We also note similar results for the random-axis division model in the FEM simulator and the case of topologically unbiased division orientations in the topological Monte Carlo simulator (Figures S6H and S5F). Both of these division mechanisms effectively remove the bias. Therefore, we can directly compare the presence or absence of bias in the FEM simulator with that of the topological simulator. Like the topological simulator, the FEM simulations closely reproduce the empirical distribution of polygonal cell shapes, and also recapitulate the drop in hexagonal frequency in the absence of

bias (Figure S6F). Additionally, as predicted by the topological simulator, the distribution of mitotic cells is noticeably altered in the FEM when cleavage plane bias is absent. The frequency of dividing heptagons declines significantly, whereas the frequencies of dividing octagons and nonagons increase (Figure S6G). Taken together, the above results suggest that the cleavage plane bias will have similar topological effects irrespective of the spatial or statistical mechanism used to generate it. Such topological effects appear to extend both to the population of cells as a whole, and also to the population of dividing cells.

The FEM simulator also provides additional geometrical results that cannot be predicted by the topological simulator, because the latter does not model cell geometry. We made three observations on the basis of the FEM simulator alone. First, we tested whether the presence or absence of T1 transitions would significantly alter our results. As implemented (l_{crit}=1/20 the average edge length), we did not find that the presence or absence of T1 transitions qualitatively changed the simulation results. Second, for simulations including T1 transitions, we tested whether simulated tissues using random axis divisions would be more prone to T1 rearrangements, relative to simulations using long-axis divisions. Indeed, we found that the frequency of T1-type transitions was more than sevenfold higher in the random-axis division case compared with the long-axis division case. Third, we found that FEM simulations using long-axis division mechanisms produce simulated tissues that are more regular in appearance (Figure

S6A,C). FEM simulations using random-axis divisions, by contrast, seem to produce more irregular and mechanically frustrated tissues (Figure S6B,D). Taken together, the above results suggest that long-axis division mechanisms may promote geometric in addition to topological regularity.

9. Geometrical analysis of cleavage plane bias:

For the special case of a regular N-sided cell surrounded by a planar hexagonal network, we can analytically compute the approximate length of the long axis for the hexagons immediately adjacent to the N-cell. For a diagram, see figures 5B-C in the text (Figure 5C is the general case). We consider an orientation for which the N-cell, *N*, has its top-most edge horizontal with respect to the observer (Figure 5A-C, 5E-F). Our analysis concentrates on the hexagon that is vertically above the N-cell, here referred to as "*M*," although the same analysis would apply to any of the other hexagons.

To compute the horizontal axis, d_m, of *M*, we first computed the internal angles of *M* and *N* (Figure 5C). From geometry, the internal angles of *N* are found as: $\alpha_n = \pi (N-2)/N$. The adjacent internal angles β_m for *M* (Figure 5C) satisfy the condition $\alpha_n + 2\beta_m = 2\pi$, from which we find $\beta_m = \pi (N+2)/(2N)$. For the case when all edges are of unit length (L=1; see Figure 5C), these internal angle constraints specify the following length for the horizontal axis of *M*: $d_m = 1 + 2\sin(\pi/N)$. For purposes of comparison with the simulation data, we have computed the approximate height of *M* in terms of the ellipse of best fit to the cell's vertices. For simplicity, we assume that the upper and lower halves of *M* are symmetrical.

To compute the vertical height (in the y-direction) of the ellipse, we used a parametric representation, where x(t) is Acos(t) and y(t) is Bsin(t). We chose a coordinate system such that the center of *M* was located at the origin. Because *M* is symmetric about its long and short axes, we were able to fit an ellipse to *M* using information from only two of its vertices: one of the two vertices at the ends of the horizontal axis, and one of the four other points. We arbitrarily chose the point (1/2, cos(π/N)) as well as the horizontal point (1/2+sin(π /N), 0). To determine the parameter A, we assumed that the ellipse must pass through (1/2+sin(π /N), 0). This constraint is equivalent to imposing a horizontal axis of d_m, which is reasonable because the ellipse is meant to represent the shape of *M*. To make use of the second constraint, we first solved for the t value, t*, when the function Acos(t) would pass through the second point (ie, when x equals 1/2). Based on t*, we solved for a B value, which along with A determines the ellipse. Over a wide range of N values, we found that this approximation agrees with a direct least-squares elliptical fit (Fitzgibbon et al., 1999) to 13 decimal places or better (the two computations may be equivalent). Therefore, using the parameters A and B, we can accurately compute the long and short axes of the ellipse of best fit. The values of A and B are the following:

$$A = \frac{1}{2} + \sin(\frac{\pi}{N}) \tag{9}$$

$$B = \frac{\cos(\frac{\pi}{N})}{\sqrt{1 - \frac{1}{(2\sin(\frac{\pi}{N}) + 1)^2}}} \tag{10}.$$

We can determine which axis of *M* (either h_m or d_m) is the longest axis for a given N value by comparing the ratio of d_m to the height of the vertical axis, h_m. This ratio (equivalent to the ratio A:B) is the following:

$$\frac{d_m}{h_m} \approx \sec\left(\frac{\pi}{N}\right)\sqrt{\sin\left(\frac{\pi}{N}\right)\left(1+\sin\left(\frac{\pi}{N}\right)\right)} \qquad (11).$$

The approximation comes from the assumption that *M* is symmetrical about its long and short axes (see above). When d_m / h_m is less than 1, h_m is the long axis. When d_m/h_m is greater than 1, h_m is the short axis. This corresponds to the case when *N* is predicted to be in the division plane position of *M*. Because the ratio d_m/h_m is a decreasing function of N in the biological range (*red*, Figure 5D), it assumes the value d_m/h_m=1 (gray, Figure 5D) at exactly one N-value. We refer to this value as the "critical point," because it determines when the long and short axes rotate by 90˚. Solving for the critical point therefore summarizes the behavior of the system. In this case, the critical point is N=6. For N values smaller than six, h_m is the short axis, which points towards *N*, just as we observe both in simulation and *in vivo*. Conversely, for N values larger than six, d_m is the short axis, and is parallel to the N-M interface.

For the more general case when *N* has edges of length L, we find a different value for the horizontal axis: d_m = L + 2sin(π/N). For this case, both the ratio d_m/h_m and the critical point depend on the L value (Figure 5D). Using an identical procedure as before, for the ellipse we find the following values for A and B:

$$A = \frac{L}{2} + \sin(\frac{\pi}{N}) \qquad (12)$$

$$B = \frac{\cos(\frac{\pi}{N})}{\sqrt{1 - \frac{L^2}{(L + 2\sin(\frac{\pi}{N}))^2}}} \quad (13).$$

Here, the ratio d_m/h_m is the following:

$$\frac{d_m}{h_m} \approx \sec\left(\frac{\pi}{N}\right)\sqrt{\sin\left(\frac{\pi}{N}\right)\left(L + \sin\left(\frac{\pi}{N}\right)\right)} \quad (14).$$

Larger L values tend to increase the critical point, whereas smaller L values tend to reduce it (Figure 5D). Given that the standard deviation is about 34% of the mean (data not shown), we wondered whether variability in L might push the critical point outside of the empirically observed range of polygonal cell shapes, making topology irrelevant. Our analysis suggests that this is extremely unlikely, because L would need to change by about 40% in order to shift the critical point by even a single polygon class (Figure 5D). To answer the question empirically, we computed an "effective" L value based on empirical hexagonal geometry. The effective L value is computed by considering the space of N-sided cells neighboring the set of all hexagonal cells. The edge length separating each N-cell/hexagonal cell pair is computed, and then divided by the average value of the remaining five edge lengths of the hexagon. Based on this simple algorithm, the effective L values for the *Drosophila* wing disc are summarized in table 1 (main text).

Although there is variance about the mean of about 40%, the average effective L value is close to one over a range of polygon classes. Therefore, the critical point may vary from cell to cell by a single polygon class, but on average it should be close to our

analytical predictions. This suggests that angular constraints are the dominant influence behind cleavage plane bias in the *Drosophila* wing disc and potentially all other monolayer cell sheets, with lesser contributions from the differential side lengths.

Supplemental references:

Bashein, G., and Detmer, P.R. (1994). Centroid of a Polygon. In Graphics Gems IV, P.S. Heckbert, ed. (San Diego, CA, Academic Press), pp. 3-6.
Fitzgibbon, A.W., Pilu, M., and Fisher, R.B. (1999). Direct least-squares fitting of ellipses. IEEE Transactions on Pattern Analysis and Machine Intelligence *21*, 476-480.
Gibson, W., and Gibson, M. (2009). Cell topology, geometry, and morphogenesis in proliferating epithelia. Current Topics in Developmental Biology *89*, 87-114.

Supplemental Figure

Figure S1.

Click here to download Supplemental Figure: Gibson_cellms_FigureS1.pdf

A Diagram for relaxation algorithm

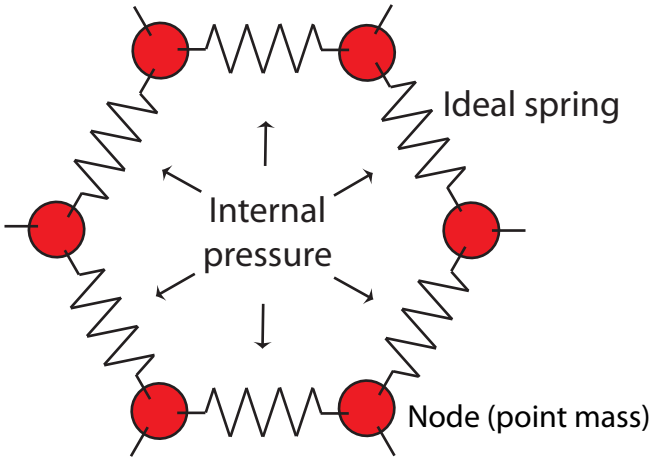

B Structural legend

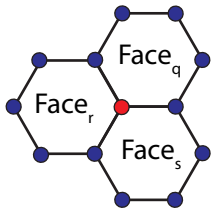

F(i) denotes the set of faces {q,r,s} to which the ith node belongs.

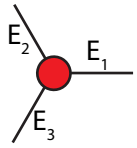

E(i) denotes the set of edges {E$_1$,E$_2$,E$_3$} impinging on node i.

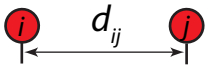

$\boldsymbol{d_{ij}}$ is the distance between nodes i and j.

C Outline of algorithmic terms

(1) Node i **feels a tensional force** T_{ij} when the distance d_{ij} between nodes i and j exceeds l_0, the spring's rest length.

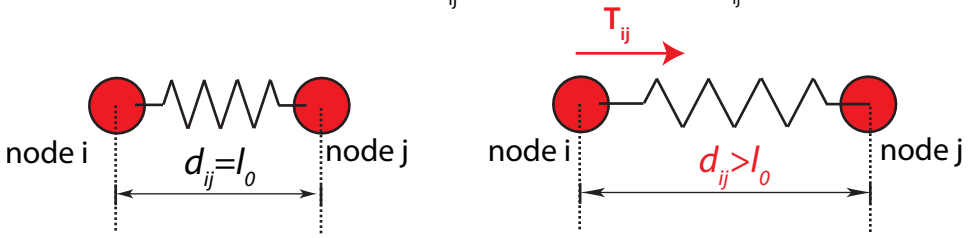

$$\left\| T_{ij} \right\| \propto (d_{ij} - l_0)$$

(2) Nodes i and j **feel a force of expansion** $P_{ij}(k)$ **due to internal pressure** from within face k.

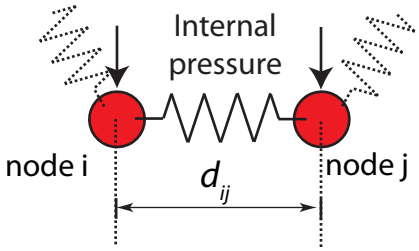

$$\left\| P_{ij}(k) \right\| \propto \frac{d_{ij}}{A_k}$$

($\boldsymbol{A_k}$ is the area of face k).

(3) A frictional force opposes the motion of node i, and is proportional to node i's velocity.

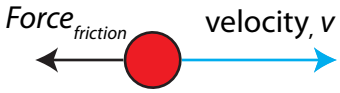

$$\left\| Force_{friction} \right\| = vC_i$$

($\boldsymbol{C_i}$ is the friction coefficient for node i).

D. Equation used to compute the equilibrium configuration

tensile force — force of expansion

$$q_i \frac{d^2}{dt^2}\left(\vec{x}_i\right) = \left[\sum_{\substack{j \in E(i) \\ k \in F(i)}} \vec{T}_{ij} + \frac{1}{2}\vec{P}_{ij}(k) \right] - C_i \frac{d}{dt}\left(\vec{x}_i\right)$$

$\mathbf{q_i}$ is the mass for the ith node — frictional force

Supplemental Figure

Click here to download Supplemental Figure: Gibson_cellms_FigureS2.pdf

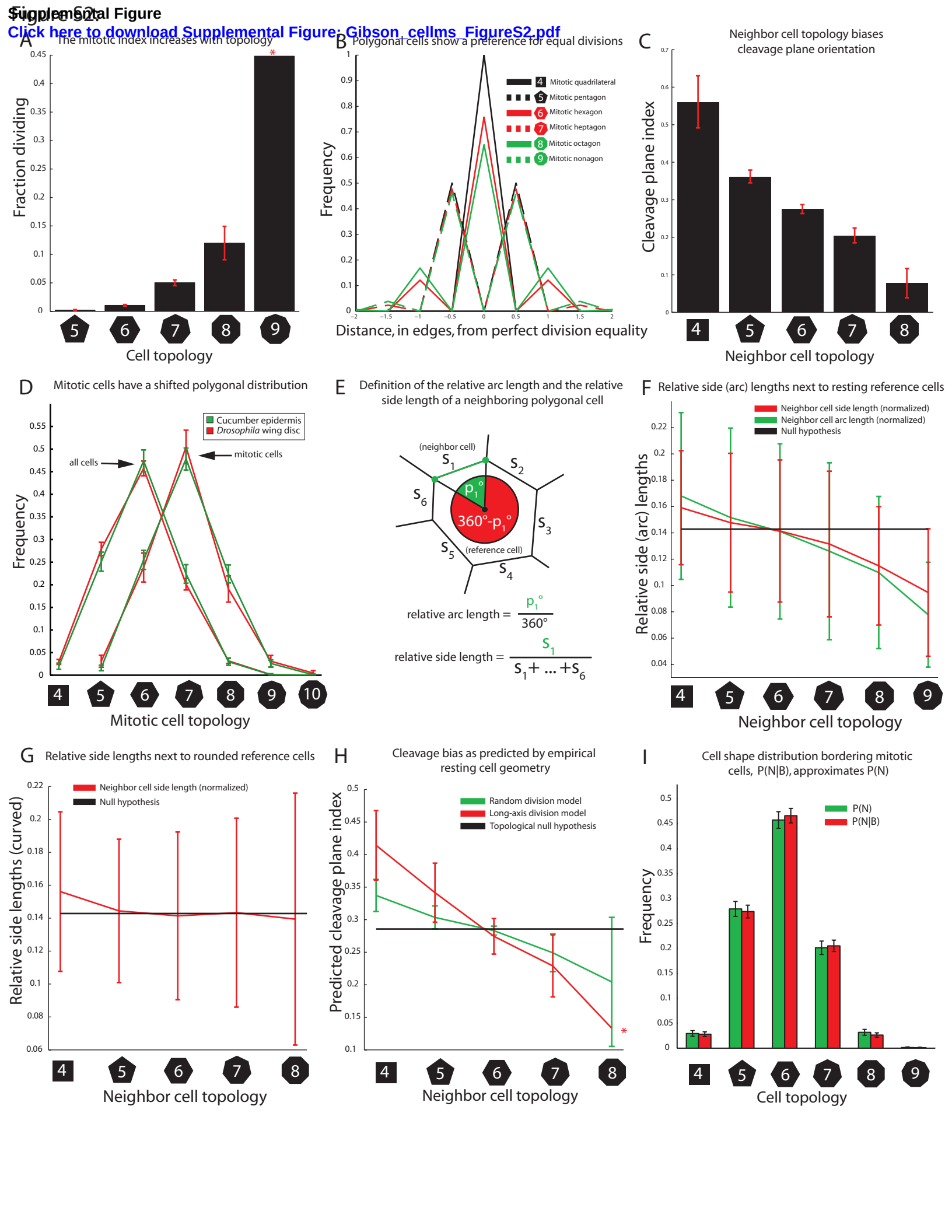

Supplemental Figure

Click here to download Supplemental Figure: Gibson_cellms_FigureS3.pdf

Figure S3:

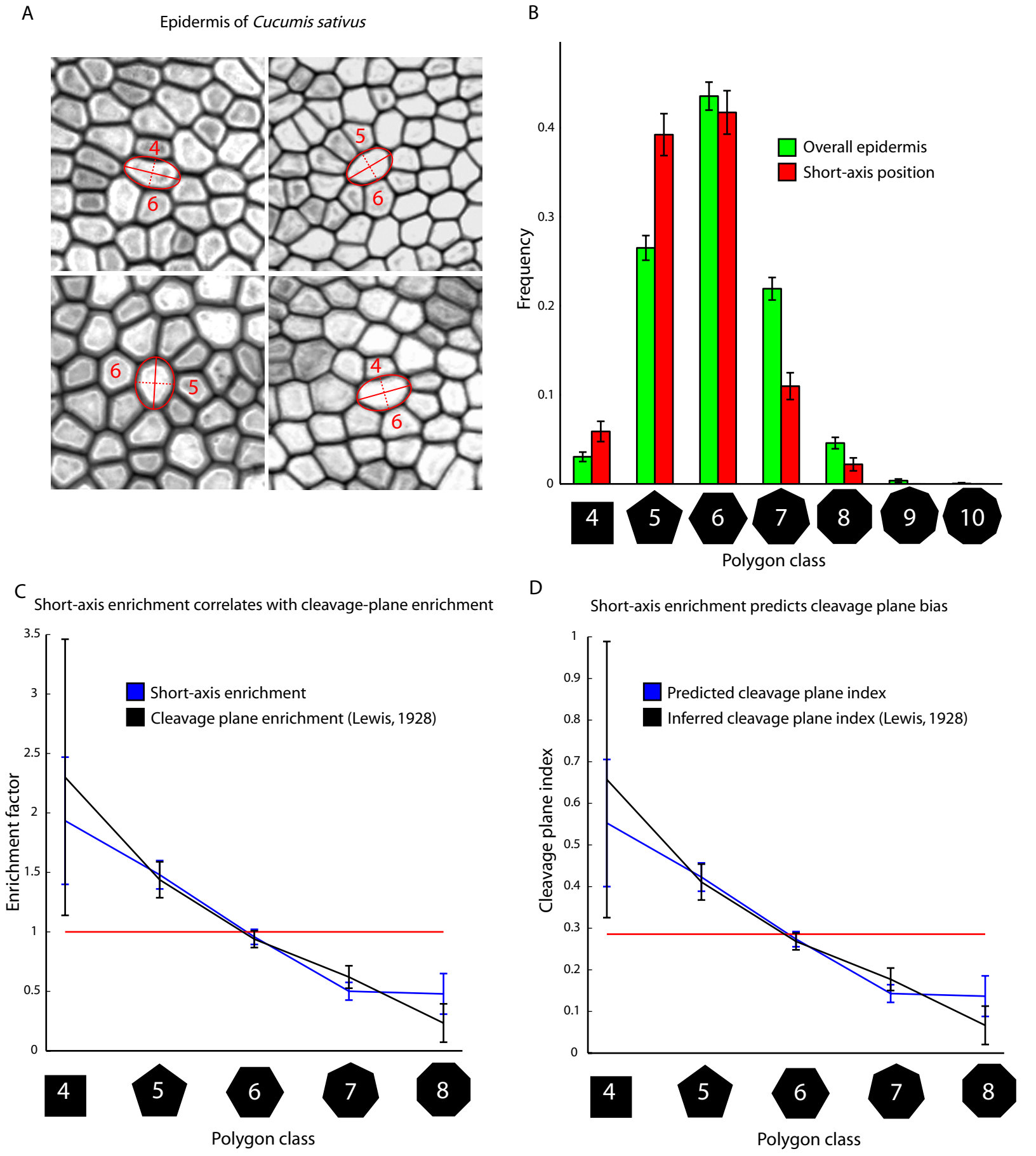

Supplemental Figure

Click here to download Supplemental Figure: Gibson_cellms_FigureS4.pdf

Figure S4:

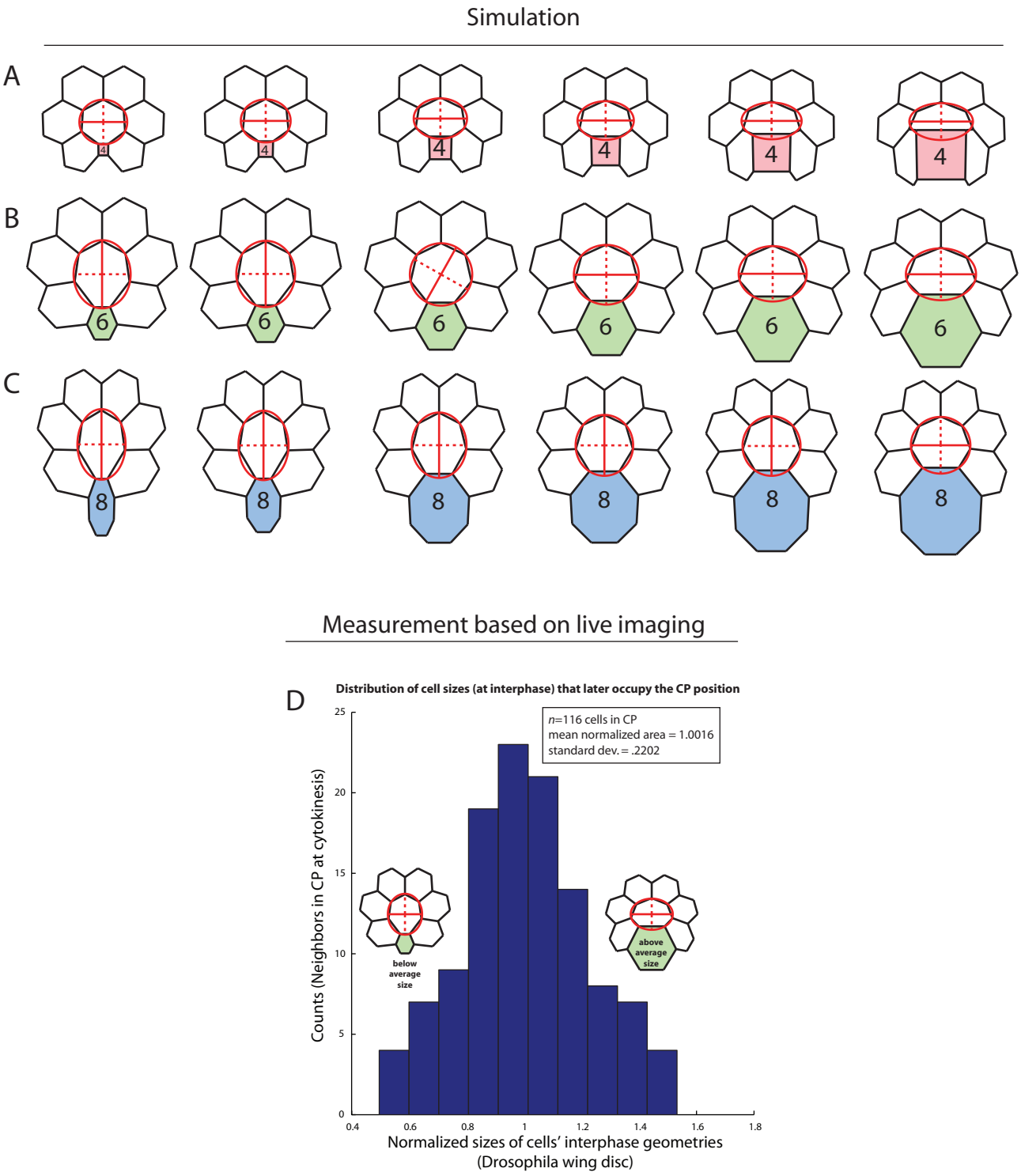

Supplemental Figure

Figure S5.

Click here to download Supplemental Figure: Gibson_cellms_FigureS5.pdf

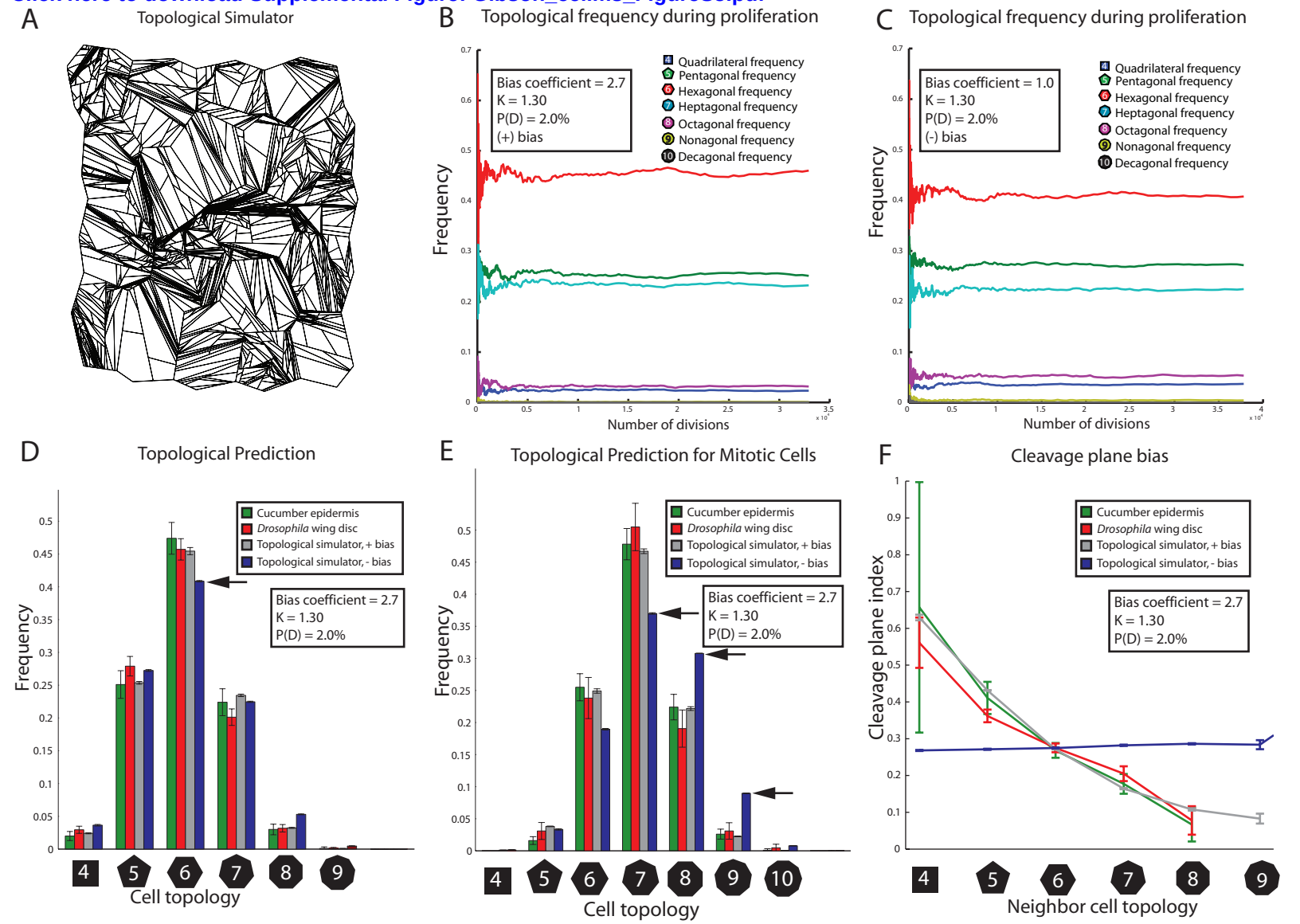

Supplemental Figure

Click here to download Supplemental Figure: Gibson_cellms_FigureS6.pdf

Figure S6:

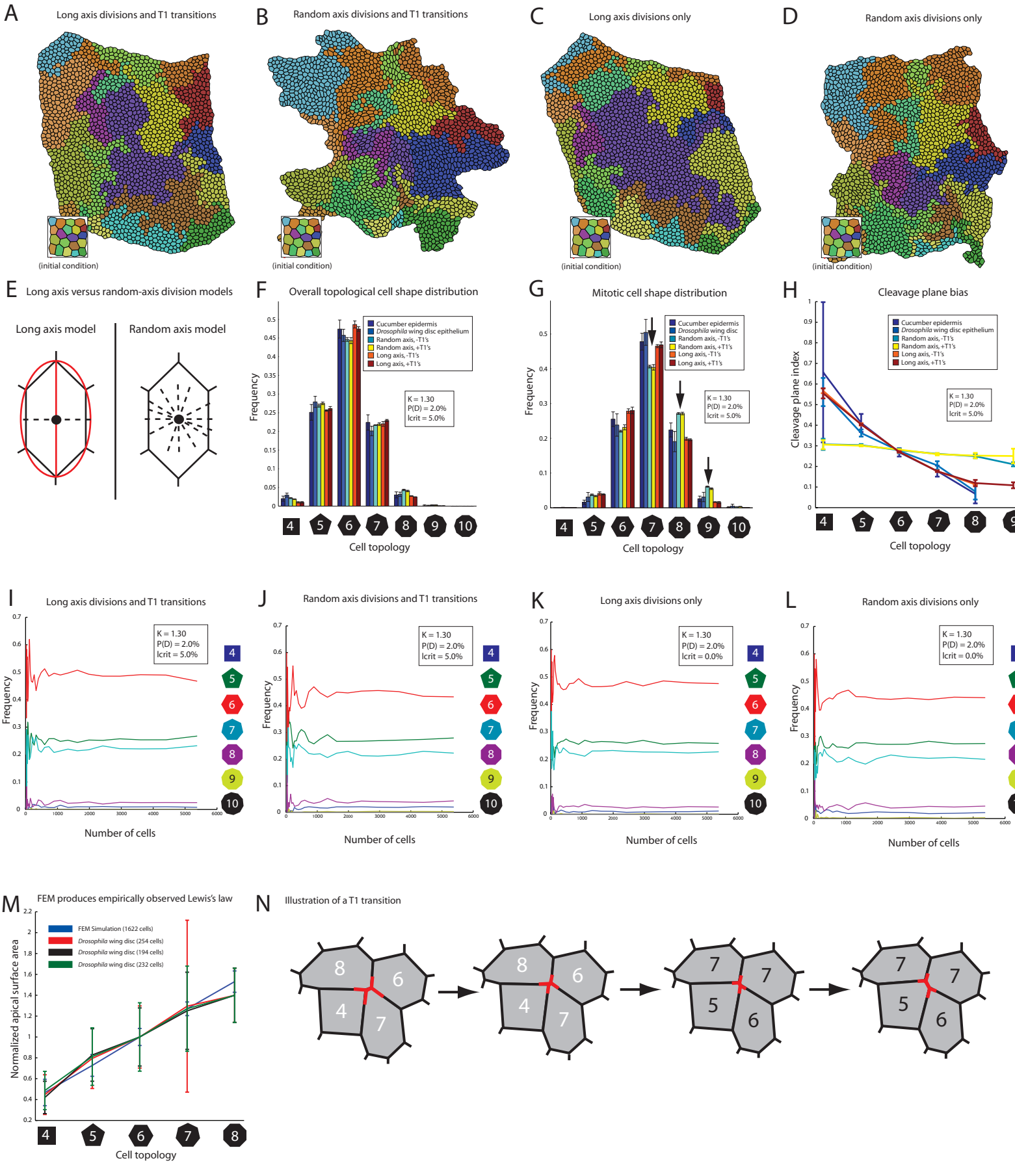

Supplemental Movies and Spreadsheets

Click here to download Supplemental Movies and Spreadsheets: Gibson_cellms_MovieS1.mp4